Lectures on HERA physics

B. Foster[1,2]

[1] H.H. Wills Physics Laboratory, University of Bristol, Tyndall Avenue, Bristol, BS8 1TL, U.K.
e-mail: b.foster@bris.ac.uk
[2] DESY, Notkestrasse 85, 22607 Hamburg, Germany.

Abstract. In these lectures I introduce the basics of HERA physics and give a survey of the major aspects, discussing in somewhat more depth the subject of low x physics.

1 Introduction

The study of deep inelastic lepton-proton scattering has produced some of the major underpinnings of the Standard Model. For example, the quark-parton model took shape in the light of the deep inelastic scattering (DIS) experiments [1] begun at SLAC in the late 1960s. Going even further back, the scattering of energetic "simple" α particles from the nuclei in a thin gold foil, carried out by Geiger and Marsden in Manchester in 1909, led to the concept of the nuclear atom [2,3] and is clearly analogous to deep inelastic lepton scattering in modern particle physics.

In my lectures I first gave an overview before covering one particular area in more detail. In the interests of producing a more coherent write-up, I have changed the original order. I first outline the HERA accelerator and detectors before discussing the theoretical techniques used to derive the basic formulae used in the study of electron-quark scattering. Then I give an overview of the main areas of HERA physics, going into somewhat more detail in one particular area, that of electron-proton scattering when the interacting quark has a low fraction of the original protons momentum, so-called "low-x" physics, and related areas such as diffraction. Here, recent theoretical developments and model building are changing our perception and improving our understanding of the very rich phenomenology arising from the many different but related channels that can be explored at HERA. I conclude with a discussion of the recent upgrades to both the accelerator and experiments in the HERA II programme and the main areas of physics that they will address.

2 Introduction to the HERA machine and experiments

HERA is a unique facility, colliding beams of electrons or positrons with protons at high energy. The protons are accelerated and stored in a ring

of superconducting magnets; until 1998 the protons were accelerated to 820 GeV and subsequently to 920 GeV. The electron or positron ring is normal conducting and beams are stored at 27.5 GeV. HERA began operation in 1992 and continuously improved its performance in successive years, as illustrated in Fig. 1, which shows the luminosity delivered to the ZEUS experiment in each year of running. Because of difficulties with the electron lifetime, the great majority of data has been taken with positron beams; only 32 pb^{-1} of electron data has been collected by ZEUS compared to a total of 148 pb^{-1} of positron data.

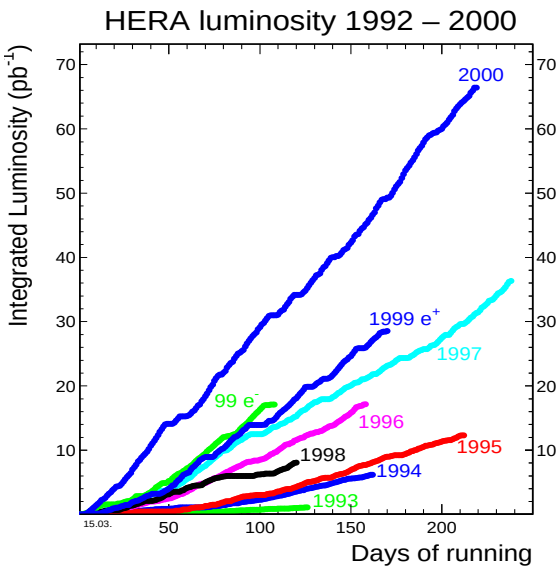

Fig. 1. The luminosity delivered to the ZEUS detector as a function of days of the run, shown separately for each year of running. A continuous improvement in the performance of HERA is evident, except for 1998, in which electrons were used rather than positrons.

There are two "general-purpose" detectors at HERA, H1 and ZEUS. In addition the HERMES experiment uses a gas target to examine polarised electron or positron-polarised proton scattering, and the HERA-B detector, designed to study CP violation in the B sector. The latter two are not discussed further in these lectures due to lack of time. Both H1 and ZEUS have a rather similar configuration, as far as possible enclosing the full solid angle with tracking detectors surrounded by calorimetry. Because of the large asymmetry between the proton and positron beam energies, the energy flow is predominantly in the proton, or "forward" direction, so that the detectors

are asymmetric, with thicker calorimetery and a higher density of tracking detectors in the forward direction. Figure 2 shows a diagram of the ZEUS detector, illustrating that its general structure, with the exception of the more complex forward instrumentation, is very typical of modern 4π detectors, such

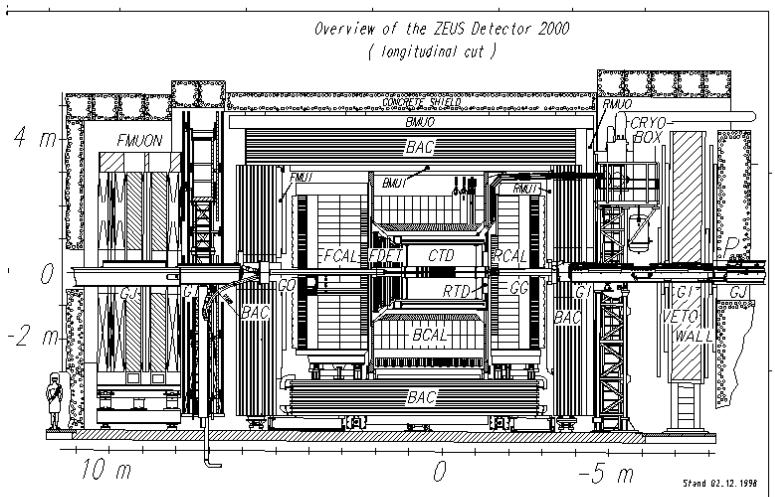

Fig. 2. A vertical section through the ZEUS detector. The black [illegible] in the very centre represent the silicon microvertex detector, which was installed in 2000. Surrounding this are the tracking detectors (CTD, FDET and RTD) and surrounding these are the uranium/scintillator calorimeters (FCAL, RCAL and BCAL). These are surrounded by an iron-scintillator backing calorimeter (BAC) which also acts as a flux return for the superconducting solenoid which surrounds the CTD. Muon chambers (FMUON, with associated toroidal magnets, BMUO and RMUO), a Veto Wall to veto off-momentum protons and a concrete shield complete the detector.

With the advent of HERA, the accessible phase space in the kinematic invariants Q^2 (the virtuality of the exchanged virtual photon) and x increased by approximately three orders of magnitude in each variable compared to what was available at earlier fixed-target experiments (see Fig. 3). This extension in kinematic range has opened up qualitatively new fields of study, both at high and low Q^2.

Since HERA is a high-energy lepton-hadron collider, it clearly gives access to hard processes in both the strong and electroweak interactions. HERA is very sensitive to the production of new particles that can be formed by the fusion of leptons and quarks, e.g. leptoquarks or many of the particles predicted by R-parity-violating supersymmetry. It is also very sensitive to any small changes in the pattern of the electroweak interaction predicted by the Standard Model. Since the colliding leptons are point-like, HERA allows complete control over the conditions of the collision by varying the Q^2, and thereby the size, of the probe. At high Q^2, HERA is a probe of the complex

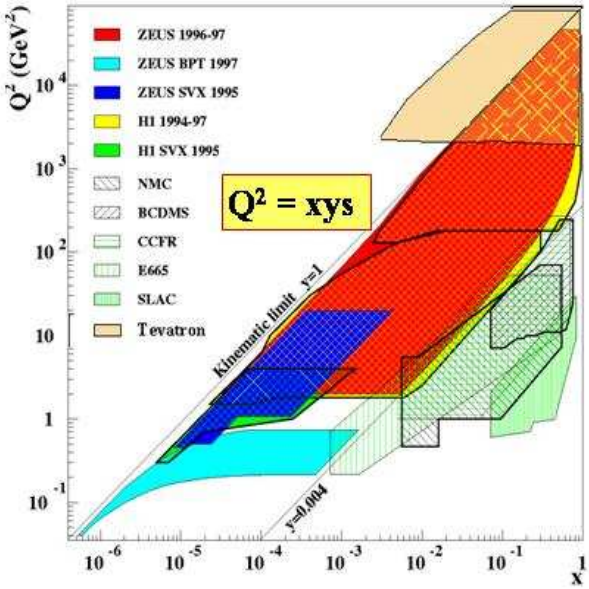

Fig. 3. The kinematic plane in x and Q^2 for experiments probing the parton distribution of the proton. The regions explored by each experiment are shown in a variety of shadings as shown in the legend. Hadron-hadron collisions are also able to measure the proton structure, predominantly at high x and high Q^2.

structure of the proton via the point-like coupling of the photon. At low Q^2, the photon becomes large and evolves its own complex structure which can be probed using the point-like interactions between its parton constituents and those of the proton. The hadronic nature of the photon under these conditions gives rise to hadron-hadron interactions with large cross sections; by also analysing diffractive interactions, in which the proton can be violently struck but remain intact, the rich structure and phenomenology of the strong interactions can be explored.

One thing that HERA physics cannot do is be simple. Unlike the situation in electron-positron annihilation, energy and quantum numbers are transferred between the colliding particles, each of which has its own conserved quantum numbers of lepton and baryon number. This means that the single annihilation energy necessary to describe most of electron-positron or high-energy hadron-hadron collisions is insufficient; two invariants are required. These can be picked from several different possibilities, the most common of which are x and Q^2. Others include W^2, the square of the energy of the hadronic final state, s, the squared centre-of-mass energy of the electron-proton system, or y, the inelasticity, which in the rest frame of the proton is the energy transferred from the electron to the proton. Only two of these variables are independent; their definitions are given in Eq. 1 in terms of the

initial- and final-state four-vectors of the electron, k and k' respectively, and the same quantities, p and p', for the proton.

$$\begin{aligned} s &= (p+k)^2 \\ Q^2 &= -q^2 = -(k'-k)^2 \\ y &= \frac{p \cdot q}{p \cdot k} \\ W^2 &= (p')^2 = (p+q)^2 \end{aligned} \tag{1}$$

Energy-momentum conservation implies that

$$x = \frac{Q^2}{2p \cdot q} \tag{2}$$

so that, ignoring the masses of the lepton and proton:

$$y = \frac{Q^2}{sx} \tag{3}$$

$$W^2 = Q^2 \frac{1-x}{x} \tag{4}$$

Another thing that one cannot expect from HERA is to discover the Higgs. HERA physics is dominated by the collisions of the lightest quarks with the lightest leptons, so that it is the worst place to look for new particles whose couplings are proportional to mass. Neither can HERA produce new particles with mass close to the centre-of-mass energy unless they have the quantum numbers of leptoquarks; a large proportion of the energy must be carried off by the final-state lepton and baryon in the t channel and is not available for the production of new particles.

Finally, it cannot be expected that HERA physics will be simple. Many of the simplest problems in QCD have already been studied in detail. The remaining ones, such as the problem of confinement, are of the highest importance but extremely difficult to study in practice, since they manifest themselves in regimes in which the strong interaction is really strong.

3 The formalism of Deep Inelastic Scattering

It is instructive to remind oneself that the basic formalism of DIS can be relatively easily derived[1] from the QED treatment of spin-$\frac{1}{2}$ – spin-$\frac{1}{2}$ scattering. It is convenient to work in a frame in which the interaction of the virtual photon with the constituents in the proton can be considered as incoherent,

[1] In my lecturers I spent considerable time in deriving many of the standard DIS equations from first principles. My approach was based on the use of the Mandelstam variables and follows closely the treatment in Chapters 6 – 10 of Halzen and Martin [4]. Only an outline of the main points is reproduced here.

i.e. the characteristic time of the $\gamma^* q$ interactions is much shorter than any interactions between the partons. A suitable frame is the infinite-momentum frame of the proton, which at HERA can be approximated by the lab. or centre-of-mass frame. In such a frame, Lorentz contraction reduces the proton to a "pancake" and time dilation increases the lifetimes of the fluctuating partons so that the proton constituents are effectively "frozen". Provided that the quarks have negligible effective mass, i.e. have small rest mass and are asymptotically free, and that $Q^2 \ll k_T^2$, then the interactions can be considered incoherent [5].

The basic process of an electron scattering incoherently from a quark is now identical to the classic QED calculation of electron-muon scattering. Writing the initial and final four-momenta of the electron as k, k' and those of the proton as p, p', the standard Feyman rules allow us to write the matrix element as

$$\mathcal{M} = -e^2 \overline{u}(k')\gamma^\nu u(k) \frac{1}{q^2} \overline{u}(p')\gamma_\nu u(p) \tag{5}$$

Using standard trace techniques and ignoring mass terms leads to

$$|\mathcal{M}|^2 = \frac{8e^4}{(k-k')^4} \left[(k' \cdot p')(k \cdot p) + [(k' \cdot p)(k \cdot p')\right] \tag{6}$$

It is very convenient to use the Mandelstam variables, s, t and u, since not only can they easily be evaluated in any frame, but also there are several useful relations between them and the more usual DIS variables of Eq. 1 that simplify the algebra. The Mandelstam variables are defined in terms of the four-vectors as:

$$s \equiv (k+p)^2 \simeq 2k \cdot p \simeq 2k' \cdot p', \tag{7}$$

$$t \equiv (k-k')^2 \simeq -2k \cdot k' \simeq -2p \cdot p', \tag{8}$$

$$u \equiv (k-p')^2 \simeq -2k \cdot p' \simeq -2k' \cdot p, \tag{9}$$

so that Eq. 6 simplifies to become

$$|\mathcal{M}|^2 = \frac{2e^4}{t^2}(s^2 + u^2) \tag{10}$$

Note that crossing, the replacement of s by t and vice-versa, leads to the well-known formula for $e^+e^- \to \mu^+\mu^-$.

The matrix element can be converted to a cross section by using the standard formula for $2 \to 2$ scattering,

$$\frac{d\sigma}{d\hat{t}} = \frac{1}{16\pi\hat{s}^2} |\mathcal{M}|^2, \tag{11}$$

to give

$$\frac{d\sigma}{d\hat{t}} = \frac{e^4}{8\pi\hat{s}^2\hat{t}^2}(\hat{s}^2 + \hat{u}^2), \tag{12}$$

where the hatted variables represent the Mandelstam variables for the subprocess in question, which for $e-\mu$ scattering are identical to the unhatted variables, but which for eq scattering are not. Considering now eq scattering, the Mandelstam variables satisfy

$$\hat{s}+\hat{t}+\hat{u}=0, \tag{13}$$

which, assuming that the quark brings a fraction x of the protons energy into the eq collision can be written as

$$x(s+u)+t=0. \tag{14}$$

Equation 12 can be converted into a double-differential cross section using the appropriate δ function to give

$$\frac{d^2\sigma}{d\hat{t}d\hat{u}}=\frac{e^4}{8\pi\hat{s}^2\hat{t}^2}(\hat{s}^2+\hat{u}^2)\delta(\hat{s}+\hat{t}+\hat{u}), \tag{15}$$

which, using the appropriate Jacobian, can be written in terms of s, t and u as

$$\frac{d^2\sigma}{dtdu}=\frac{2\pi\alpha^2 x e_q^2}{s^2t^2}(s^2+u^2)\delta(t+x(s+u)), \tag{16}$$

where α is the fine-structure constant, $\alpha=e^2/4\pi$ and e_q is the charge of the struck quark in units of the electron charge. We can then write the total ep cross section as the incoherent sum of all possible eq scatters, i.e.

$$\left(\frac{d^2\sigma}{dtdu}\right)_{ep\to eX}=\sum_i\int f_i(x)\left(\frac{d^2\sigma}{dtdu}\right)_{eq_i\to eq_i}dx, \tag{17}$$

where $f_i(x)$ is the density distribution inside the proton of quark i between x and $x+dx$.

We can also treat the overall inclusive DIS process $ep\to eX$ from first principles using the Feynman rules provided that we take cognizance of the fact that the proton is not a point-like particle. To do that, we parameterise the proton vertex contribution to the matrix element in the most general way possible in terms of a hadronic tensor, $W_{\mu\nu}$, given by

$$W_{\mu\nu}=\left(-g_{\mu\nu}+\frac{q_\mu q_\nu}{q^2}\right)F_1(x,Q^2)+\frac{\hat{p}_\mu\hat{p}_\nu}{p\cdot q}F_2(x,Q^2)-i\varepsilon_{\mu\nu\alpha\beta}\frac{q^\alpha q^\beta}{2p\cdot q}F_3(x,Q^2) \tag{18}$$

where

$$\hat{p}_\mu=p_\mu-\frac{p\cdot q}{q^2}q_\mu, \tag{19}$$

and F_1, F_2 and F_3 are "structure functions" describing, in the most general way compatible with relativistic invariance, the unknown structure of the proton. The antisymmetric ε tensor shows that the F_3 structure function is

parity violating; we will ignore it for the moment, restricting the discussion to low-Q^2 neutral current events where the effects of W and Z exchange can be neglected. Contracting $W_{\mu\nu}$ with the leptonic tensor used to obtain Eq. 6 leads to

$$\frac{d^2\sigma}{dtdu} = \frac{4\pi\alpha^2}{s^2t^2(s+u)}\left[(s+u)^2 xF_1(x,Q^2) - suF_2(x,Q^2)\right], \tag{20}$$

which can now be compared with Eq. 17. Substituting Eq. 16 and evaluating the integral using the δ function leads to

$$\left(\frac{d^2\sigma}{dtdu}\right)_{ep\to eX} = \sum_i f_i(x)\frac{2\pi x\alpha^2 e_{q_i^2}}{s^2t^2}\frac{(s^2+u^2)}{s+u}. \tag{21}$$

Comparison with the right-hand side of Eq. 20 shows that, since s and u are continuous variables, the two equations can only be consistent if the coefficients of the s^2+u^2 and su terms are equal, i.e.

$$2xF_1(x,Q^2) = \sum_i f_i(x)xe_{q_i}^2 = F_2(x,Q^2). \tag{22}$$

This relation between F_1 and F_2 is known as the Callan-Gross [6] relation. Equation 22 also implies that F_2 is a function of x only, a phenomenon known as "scaling". This was clearly observed in the original SLAC experiments, as shown in Fig. 4 and is also clearly visible in the HERA data shown in Fig. 5 at similar values of x. However, when one looks at other values of x, it is clear that scaling becomes progressively more and more violated.

The phenomenon of scaling violation is one of the clearest manifestations of Quantum Chromodynamics and is caused by gluon radiation from the struck quark. This radiation is accompanied by a transfer of energy to the emitted gluon, which leads to a shift of the average quark x to lower values. The emitted gluon can also split into further quark-antiquark pairs which are also at low x. Thus, since the gluon bremsstrahlung depends on Q^2, the cross section develops a strong Q^2 and x dependence. This can conveniently be taken into account by re-writing Eq. 20 as a function of x and Q^2 using the Jacobian, $(s+u)/x$, as

$$\begin{aligned}\frac{d^2\sigma}{dxdQ^2} &= \frac{2\pi\alpha^2}{xQ^4}\left[2\frac{(s+u)^2}{s}xF_1(x,Q^2) - 2\frac{u}{s}F_2(x,Q^2)\right] \\ &= \frac{2\pi\alpha^2}{xQ^4}\left[2xy^2F_1 + 2(1-y)F_2\right],\end{aligned} \tag{23}$$

where we have used the identity

$$y \equiv \frac{p\cdot q}{p\cdot k} = \frac{s+u}{s}. \tag{24}$$

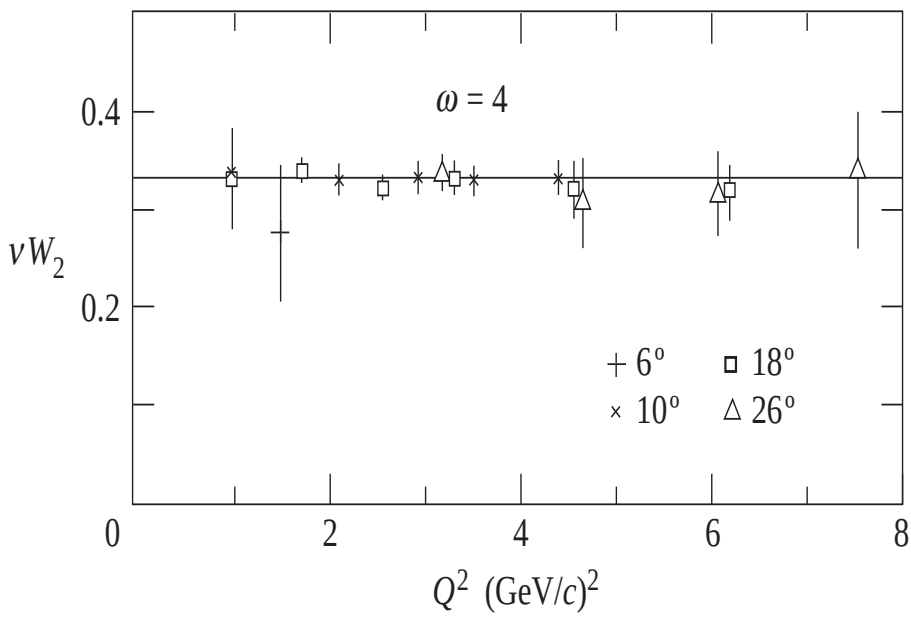

Fig. 4. The $\nu W_2(\equiv F_2)$ structure function at $\omega = 1/x = 4$ as a function of Q^2 as measured by the SLAC-MIT group [7]. Data taken at four different scattering angles are shown. All data is consistent with being independent of Q^2.

Rearranging and introducing the longitudinal structure function $F_L = F_2 - 2xF_1$ gives

$$\frac{d^2\sigma}{dxdQ^2} = \frac{2\pi\alpha^2}{xQ^4}\left[-y^2F_L + \{1 + (1-y)^2\}F_2\right]. \tag{25}$$

The longitudinal structure function is zero in the quark-parton model since the quarks have zero transverse momentum. Gluon bremsstrahlung however develops a non-zero p_t, leading to non-zero values of F_L.

Consolidating, we can re-introduce the parity-violating xF_3 term and write down the most general spin-averaged form for the cross-section as

$$\begin{aligned}\frac{d^2\sigma}{dxdQ^2} &= \frac{2\pi\alpha^2}{xQ^4}(1+\delta)\left[Y_+ \cdot F_2(x,Q^2)\right.\\ &- \left. y^2F_L(x,Q^2) \pm Y_- \cdot xF_3(x,Q^2)\right],\end{aligned} \tag{26}$$

where the $\pm$ before xF_3 is taken as positive for electron scattering and negative for positron scattering, $Y_\pm$ are kinematic factors given by

$$Y_\pm = 1 \pm (1-y)^2, \tag{27}$$

and δ is the QED radiative correction.

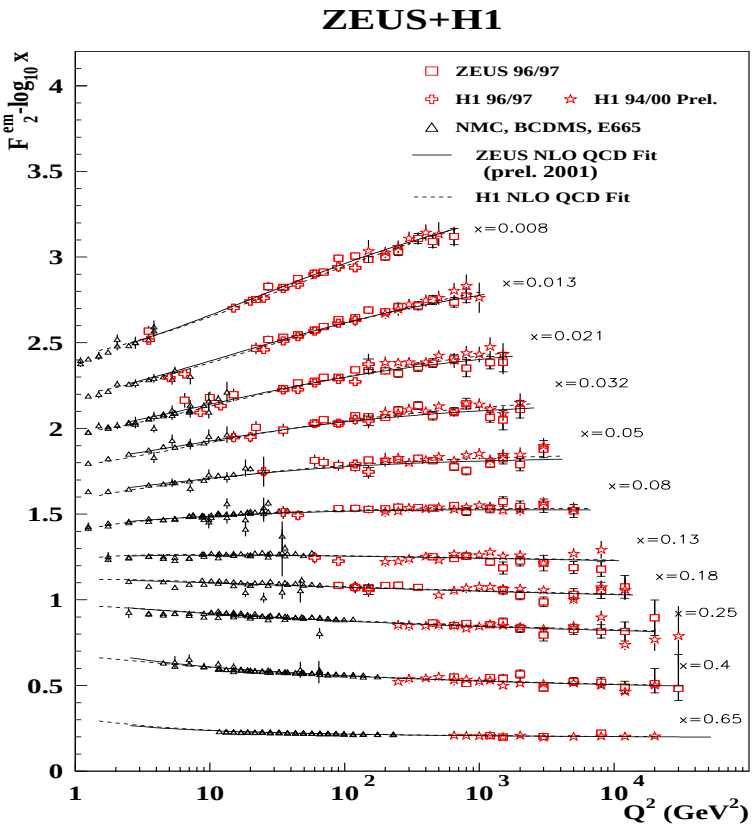

Fig. 5. The F_2 structure function as measured by the H1 and ZEUS experiments for bins at high x as a function of Q^2. The bins centred around $x = 0.25$ are where scaling was originally observed in the SLAC experiments. Clear scaling violation is observed in the HERA data outside this region, particularly at lower x.

The F_2 structure function can be expressed, in the "DIS scheme" of renormalization [8] in a particularly simple way as

$$F_2(x, Q^2) = \sum_{i=u,d,s,c,b} A_i(Q^2) \left[x q_i(x, Q^2) + x \overline{q}_i(x, Q^2). \right] \tag{28}$$

The parton distributions $q_i(x, Q^2)$ and $\overline{q}_i(x, Q^2)$ refer to quarks and antiquarks of type i. For $Q^2 \ll M_Z^2$, where M_Z is the mass of the Z^0 boson, the quantities $A_i(Q^2)$ are given by the square of the electric charge of quark or antiquark i. Similarly,

$$xF_3(x, Q^2) = \sum_{i=u,d,s,c,b} B_i(Q^2) \left[x q_i(x, Q^2) - x \overline{q}_i(x, Q^2). \right] \tag{29}$$

The full forms for the A and B terms are:

$$A_i(Q^2) = e_i^2 - 2e_i c_V^e c_V^i P_Z + ({c_V^e}^2 + {c_A^e}^2)({c_V^i}^2 + {c_A^i}^2){P_Z}^2, \tag{30}$$
$$B_i(Q^2) = \quad -2e_i c_A^e c_A^i P_Z + 4c_V^e c_V^i c_A^e c_A^i {P_Z}^2, \tag{31}$$

where

$$P_Z = \frac{Q^2}{Q^2 + M_Z^2} \tag{32}$$
$$c_V^i = T_3^i - 2e_i \sin^2\theta_W \tag{33}$$
$$c_A^i = T_3^i \tag{34}$$
$$T_3^i = +\frac{1}{2} \text{ for } i = \nu, u, c, t \tag{35}$$
$$= -\frac{1}{2} \text{ for } i = e, d, s, b \tag{36}$$

4 The HERA DIS data

4.1 The F_2 structure function at medium and high Q^2

The determination of the structure functions of the proton is a delicate and painstaking process requiring an excellent understanding of the H1 and ZEUS detector response. This understanding has progressed to the extent that the accuracy of the HERA data [9–11] is equal to that of the fixed-target experiments in the kinematic range explored by them. Of course, the HERA data also extends into a much larger region of x and Q^2 and matches well onto the fixed-target data in the region of overlap. This has already been exhibited in Fig. 5 for the higher x bins, and is further illustrated in Fig. 6 for the lower x bins, where the large scaling violations are even more obvious. The rapid rise of the structure function at low x can be clearly seen in Fig. 7, which shows F_2 in three Q^2 bins as a function of x.

4.2 Next-to-leading-order QCD fits

The precise measurement of the proton structure at low x at HERA is very sensitive both to the details of the evolution in QCD of the density of gluons and to the value of the strong coupling constant, α_s, which determines the probability of gluon emission. This sensitivity has been exploited by both ZEUS and H1. Each experiment has made a global QCD fit to its own data plus some or all of the fixed-target DIS data. There is reasonably good agreement in general terms between the experiments, although each experiment has a rather different fit procedure as well as a different choice of the fixed-target data. The quality of the fits in both experiments is excellent, as demonstrated by the curves shown in Figs. 5 - 7. The results for the density of the gluon are shown in Fig. 8.

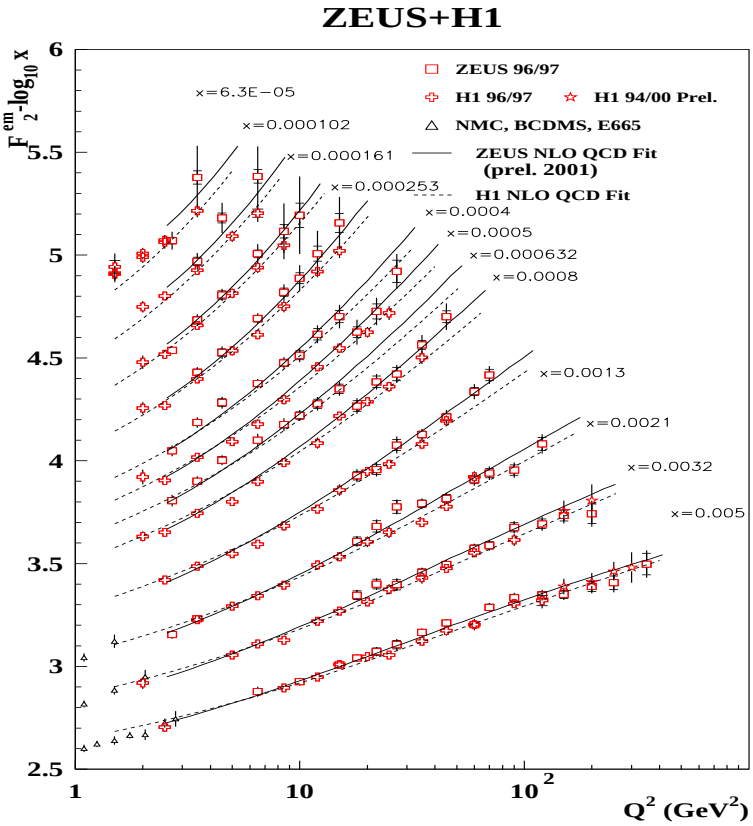

Fig. 6. The F_2 structure function as measured by the H1 and ZEUS experiments for bins at low x as a function of Q^2.

I now use the ZEUS NLOQCD fit to illustrate some points of interest. Figure 9 illustrates the evolution of the gluon density and that of the sea as a function of Q^2. While at medium Q^2 the sea density lies below that of the gluon and follows its shape, at low Q^2 it is higher than the gluon. This makes the normal interpretation, that the sea is driven by gluon splitting, rather difficult to maintain.

Figure 10 shows that F_L also begins to behave strangely at low Q^2, becoming very flat and at the lowest values of Q^2 becoming negative, although the size of the uncertainties still allow it in principle to remain positive. The gluon density, which is directly related to F_L in QCD, certainly becomes negative, which is somewhat difficult to interpret in QCD. However, it is not an observable, whereas F_L is, so that the tendency for F_L to become negative at low Q^2 implies a break-down in the QCD paradigm. We will return to this discussion in Section 5.3. The quality of the HERA data is now so high that it alone can give constraints on the parton densities scarcely less good than

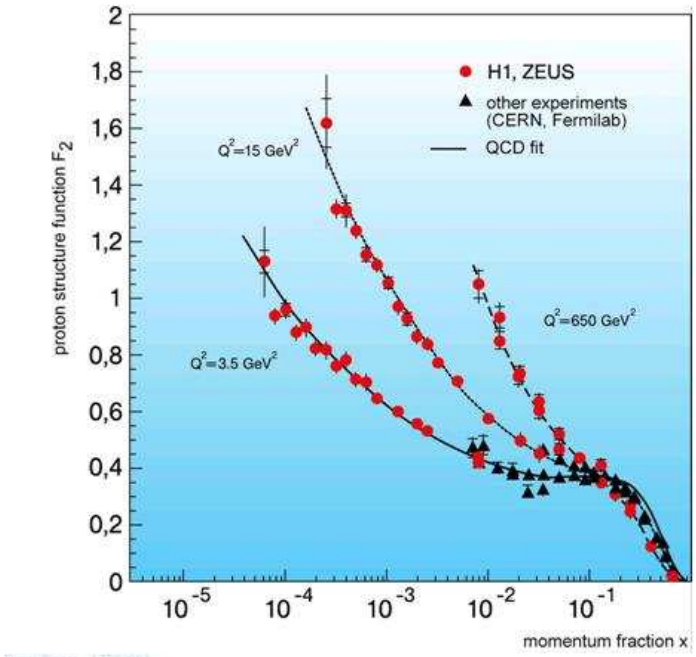

Fig. 7. H1 and ZEUS data on the F_2 structure function shown in three bins of Q^2 as a function of x. The steep rise of the structure function at low x is clearly apparent.

the fits that include also fixed-target and other data. However, it is necessary to make

some simplifying assumptions, particularly for the high-x valence behaviour, in such fits. The results are illustrated in Fig. 11, which shows the gluon density arising from such a fit, with its associated uncertainty band, in comparison with the result from the standard fit; the general behaviour is similar, with a somewhat larger uncertainty, particularly at low Q^2.

4.3 The determination of α_s at HERA

Another output of the NLOQCD fit is a value of α_s; the results from the two experiments are shown in Fig. 12, labelled as "NLO-QCD fit". The value obtained by ZEUS is

$$\alpha_s(M_Z^2) = 0.1166 \pm 0.008 \pm 0.0032 \pm 0.0018,$$

where the uncertainties derive from statistical and other uncorrelated experimental uncertainties, correlated experimental uncertainties, normalisation uncertainties and the error related to omissions and simplifications in the

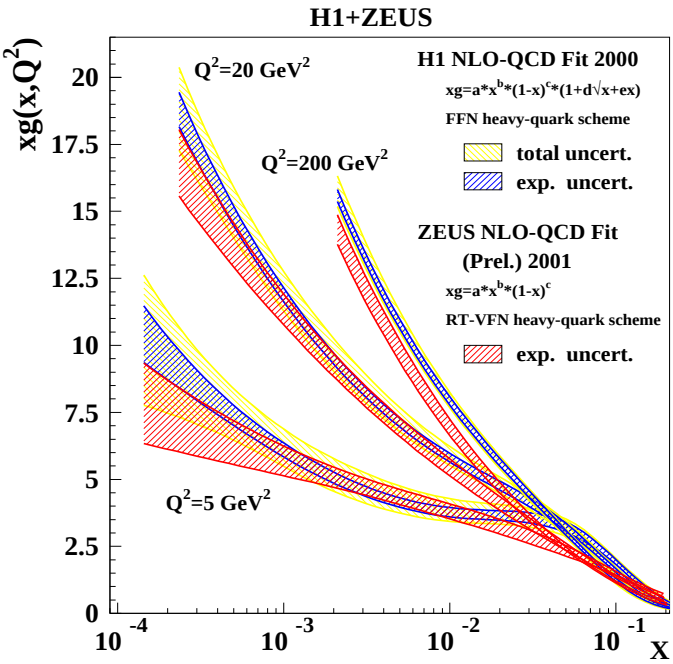

Fig. 8. The gluon density in the proton as measured by ZEUS (red shaded band) and H1 [10] (yellow and blue shaded bands) as a function of x in three bins of Q^2. The functional form used by the two collaborations in the gluon fit is somewhat different and is shown in the legend.

NLOQCD model. The value H1 obtain from their fit to their and the BCDMS data is

$$\alpha_s(M_Z^2) = 0.1150 \pm 0.0017^{+0.0009}_{-0.0005} \pm 0.005,$$

where the first error source takes account of all experimental uncertainties, the second takes account of the construction of the NLOQCD model and the final uncertainty results from the variation in the factorisation and renormalisation scale. The values of α_s obtained by the two experiments are in good agreement.

Also shown in Fig. 12 are a variety of other high-precision measurements of α_s that can be made at HERA using a variety of techniques. These include classic methods such as the rate of dijet + proton-remnant production compared to that of single jet plus remnant, the subjet-multiplicity evolution inside jets and the shape of jets. Many of these give excellent precision, comparable to the world average [12,13]. The dominant uncertainty is usually theoretical and arises from the lack of predictions at next-to-next-to-leading order.

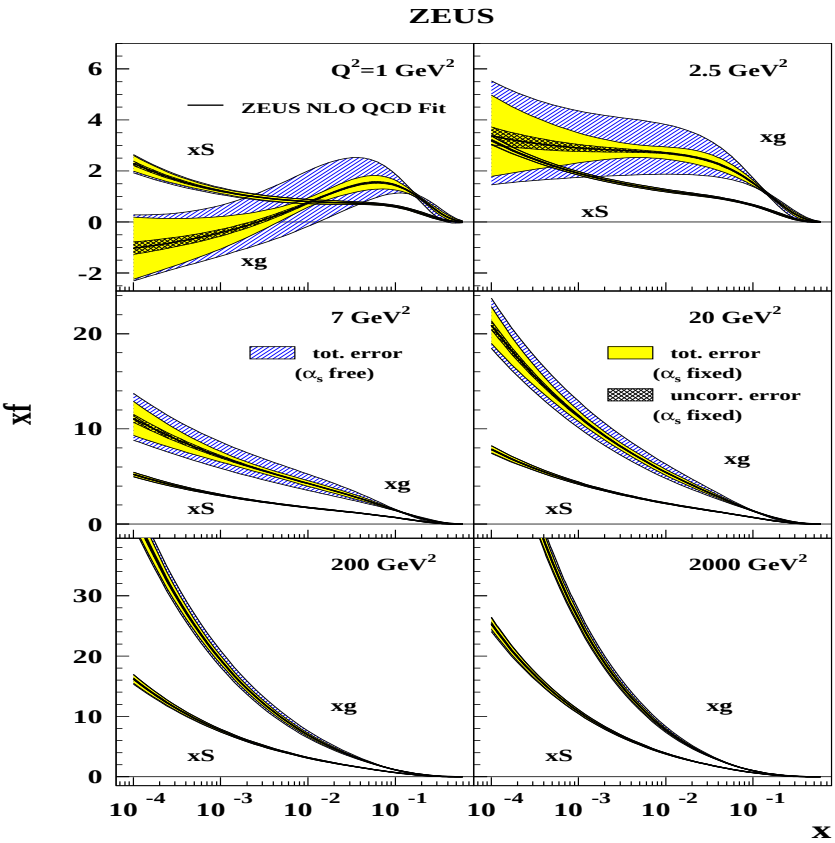

Fig. 9. The gluon density in the proton compared to that of the quark-antiquark sea in bins of Q^2 as a function of x.

4.4 The charm-quark structure function, F_2^c

In addition to the fully inclusive structure functions discussed above, both ZEUS and H1 can identify that fraction of F_2 that arises from charm production, F_2^c. This is achieved by looking for the decay mode $D^* \to D\pi$, in which, because the mass difference between the D^* and D is only just larger than the pion mass, the daughter pion has a very small momentum. The mass difference between the D^* candidate and the D candidate can therefore be measured very accurately, allowing sufficient suppression of the combinatorial background that the charm signal can be cleanly identified. The structure function can then be unfolded from the measured differential cross section using models to correct for the unmeasured parts of the phase space. The measurements of the semi-inclusive charm structure function, F_2^c, made by both experiments [14,15] using this technique are shown in Fig. 13.

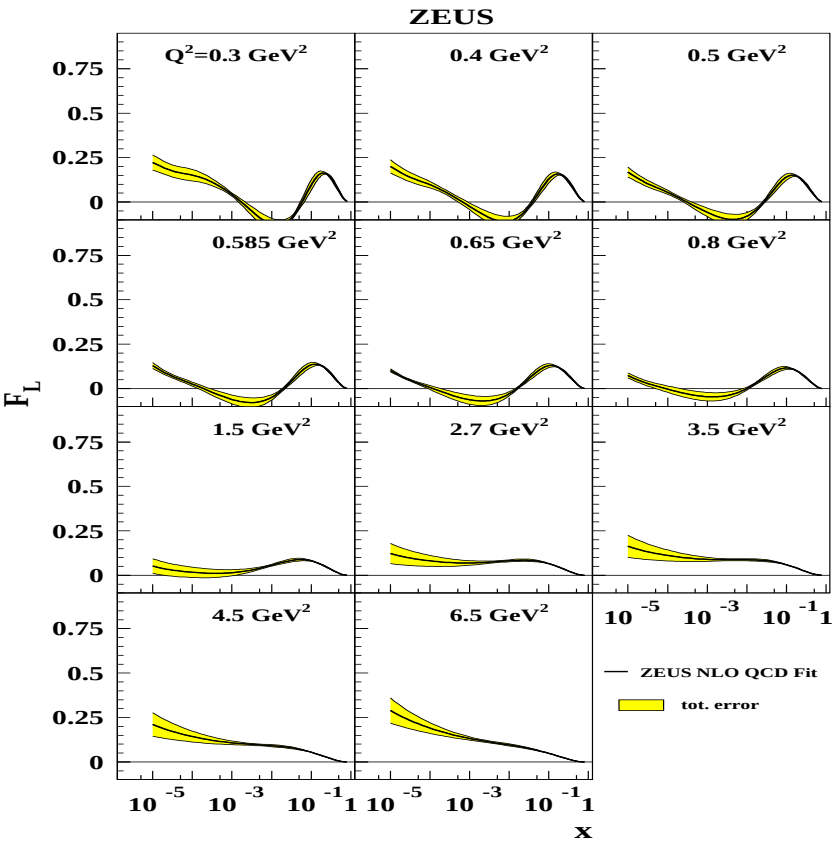

Fig. 10. The F_L structure function as predicted by the ZEUS NLOQCD fit as a function of x in bins of Q^2.

The data is still of rather limited statistical precision. Since the charm quark is produced predominantly via boson-gluon fusion, F_2^c is driven by the gluon density and thus rises steeply as x falls.

4.5 The F_L structure function

Since in principle both F_2 and F_L are unknown functions that depend on x and Q^2, the only way in which they can be separately determined is to measure the differential cross section at fixed x, Q^2 and at different values of y, since as shown in Eq. 26, the effect of F_L is weighted by y^2 whereas F_2 is weighted by $1 + (1 - y)^2$. However, since $Q^2 = sxy$, fixed x and Q^2 implies taking measurements at different values of s. This can certainly in principle be accomplished by reducing the beam energies in HERA. However, the practical difficulties for the experiments and the accelerator inherent in reducing either the proton or electron beam energy, or both, by a factor sufficient to permit

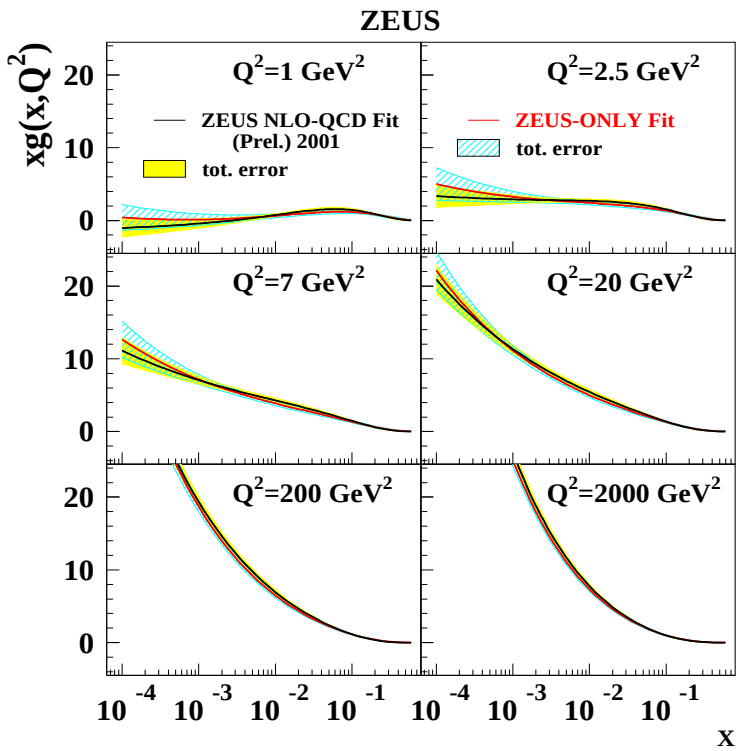

Fig. 11. The gluon density as a function of x in Q^2 bins from an NLOQCD fit using only ZEUS data.

an accurate measurement of F_L mean that it has not to date been attempted. An alternative way to achieve the same end is to isolate those events in which the incoming lepton radiates a hard photon in advance of the deep inelastic scattering, thereby reducing the effective collision energy. Unfortunately, the acceptance of the luminosity taggers typically used to detect such photons is sufficiently small and understanding the acceptance sufficiently difficult that no result has been obtained as yet.

Figure 16: The gluon distribution from the NLOQCD fit to ZEUS data alone

In the absence of any direct determination, the H1 collaboration has used events at very large values of y to make an indirect measurement of F_L. The determinations of F_2 rely on the fact that most of the measurements are made at values of y sufficiently small that the effects of F_L are negligible; at higher y, a QCD estimate of F_L, which is normally a small fraction of F_2, is subtracted. The H1 collaboration inverts this procedure by isolating kinematic regions in which the contribution of F_L is maximised and then subtracts off an estimate of F_2 extrapolated from lower y.

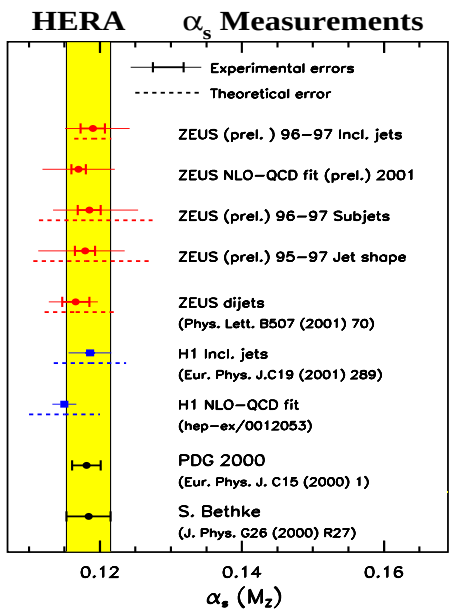

Fig. 12. Values of the strong coupling constant as determined at HERA. Each different measurement is displaced vertically for ease of visibility; each value arises from a different method as briefly indicated in the legend. The reference for published results is shown below the method label. The world average as calculated by the Particle Data Group[12] and by Bethke [13] are shown at the bottom of the figure.

The method used by H1 employs the derivatives of the reduced cross section with respect to $\ln y$. The reduced cross section can be expressed as

$$\frac{xQ^4}{2\pi\alpha^2 Y_+ \cdot (1+\delta)} \frac{d^2\sigma}{dxdQ^2} = \sigma_r$$
$$= F_2(x,Q^2) - \frac{y^2}{Y_+} F_L(x,Q^2), \tag{37}$$

which, when differentiated leads to

$$\frac{\partial \sigma_r}{\partial \ln y} = \frac{\partial F_2}{\partial \ln y} - \frac{2y^2(2-y)}{Y_+^2} F_L - \frac{y^2}{Y_+} \cdot \frac{\partial F_L}{\partial \ln y} \tag{38}$$

which gives improved sensitivity to F_L via the stronger y dependence at the cost of involving derivatives of σ_r, F_2 and F_L, the quantity to be measured. It is instructive to consider various restrictions:

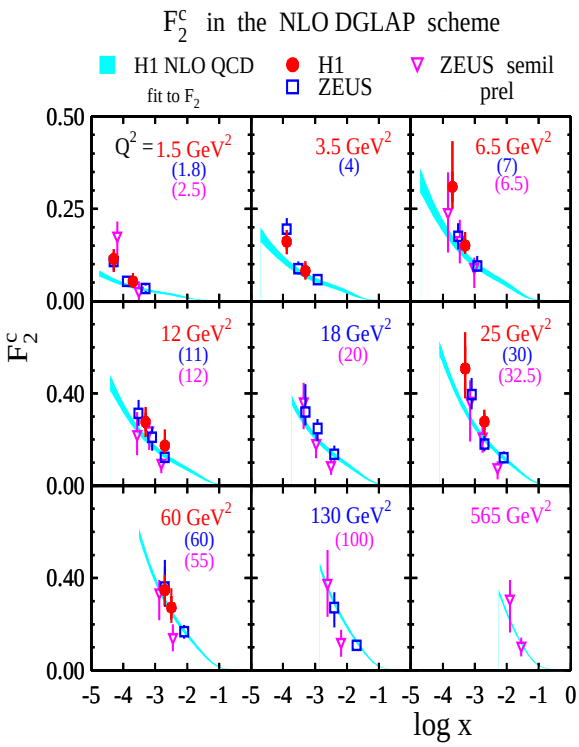

Fig. 13. Values of the charm structure function, F_2^c from the H1 and ZEUS experiments in bins of Q^2 as a function of $\ln x$. The blue squares show the ZEUS using the $D^* \to K\pi\pi_s$ decay mode, whereas the purple triangles show a ZEUS determination using the semileptonic decay of the D. The shaded curves show the predictions from the NLO QCD fit to the inclusive F_2 data by H1.

- Small y - here $\partial\sigma_r/\partial \ln y \sim \partial F_2/\partial \ln y$. For low x, F_2 can be well approximated by:

$$F_2 \propto x^{-\lambda} \propto y^{\lambda} \tag{39}$$

so that:

$$\frac{\partial F_2}{\partial \ln y} = \lambda y^{\lambda} \tag{40}$$

which can be expanded as:

$$\frac{\partial F_2}{\partial \ln y} \propto \lambda e^{\lambda \ln y} \sim \lambda(1 + \lambda \ln y \ldots) \tag{41}$$

provided $\lambda \ln y$ is small. From this it is clear that $\partial\sigma_r/\partial \ln y$ is linear in $\ln y$;

- $F_L = 0$ - for all y, $\partial\sigma_r/\partial \ln y$ is linear in $\ln y$ for the same reason as above;
- $F_L \neq 0$ and large y - $\partial\sigma_r/\partial \ln y$ is non-linear in $\ln y$ and the deviations are proportional to F_L and its logarithmic derivative;

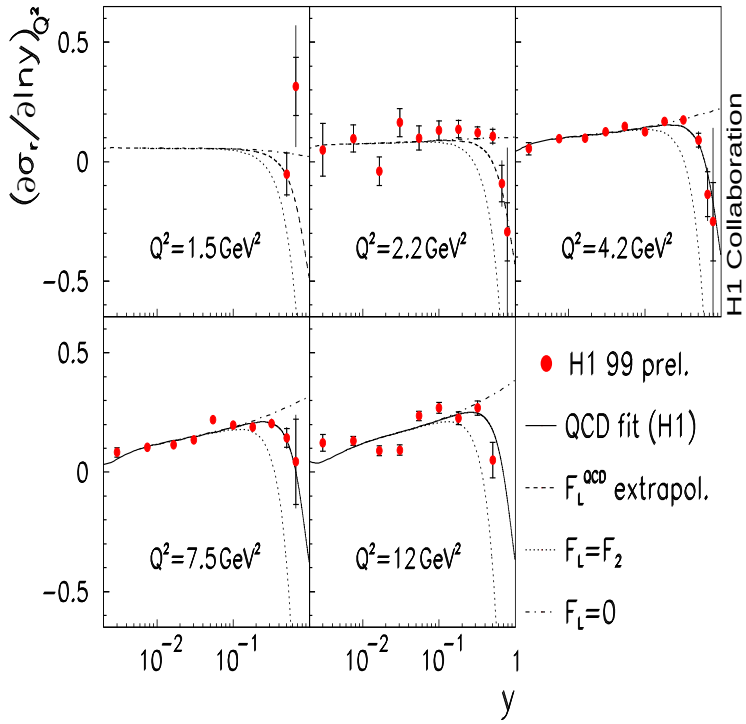

Fig. 14. The logarithmic derivative $\frac{\partial\sigma_r}{\partial \ln y}$ as a function of y in Q^2 bins. The curves represent the measurement of the derivative of the QCD fit with the different assumptions about F_L as shown in the legend.

Figure 8: Measurement of the derivative $(\partial\sigma_r/\partial \ln y)_{Q^2}$ with the different assumptions about F_L fit to the H1 96/97 data for $y < 0.35$ and $Q^2 \geq 3.5$ GeV^2 calculated with different assumptions on F_L. The inner error bars represent the statistical errors and the total error bars the statistical and systematical errors, added in quadrature.

These features can be seen in the preliminary H1 data of Fig. 14. At the largest values of y, the deviation from linearity implies that F_L is non-zero. Although it is in principle possible to solve the differential equation for F_L implied by Eq. 38, in practice the data are insufficiently precise and the QCD expectation is that the derivative of F_L is negligible. The uncertainty in this assumption is included in the systematic error.

The results are shown in Fig. 15, together with earlier determinations from SLAC [16], NMC [17] and BCDMS [18,19]. The curve is the result of an NLO QCD fit to the H1 data deriving from the F_2 determination, i.e. by deriving the gluon and quark distributions from scaling violations and then

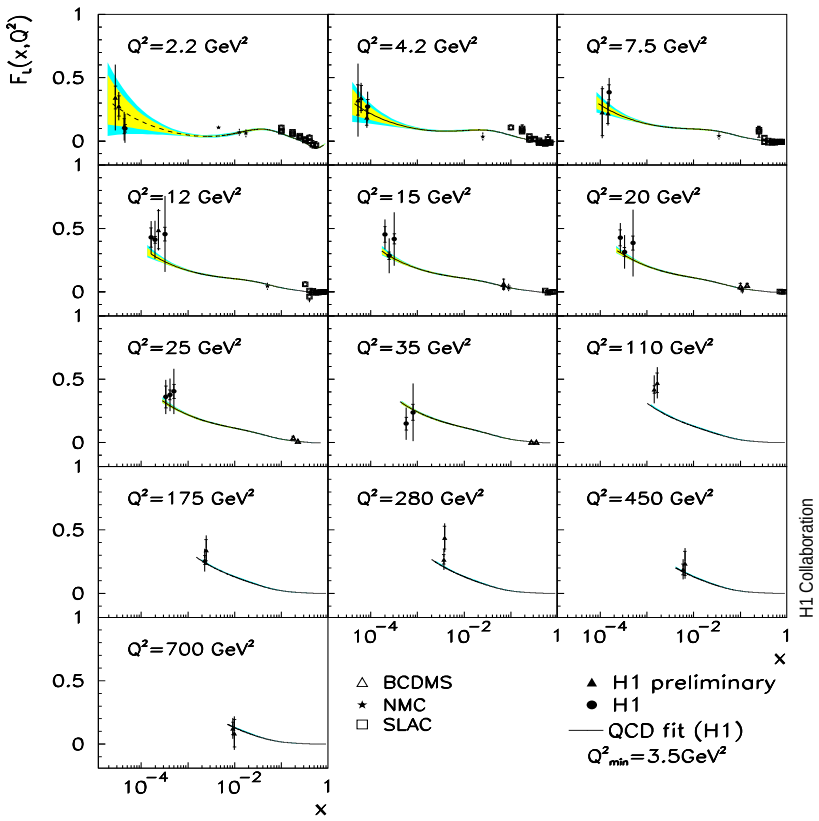

Fig. 15. Preliminary H1 estimate of F_L. The F_L values obtained are plotted in Q^2 bins as a function of x. Also shown are earlier bins at higher x from the SLAC and NMC experiments. The curves with error bands are the predictions of the H1 NLO QCD fit.

Figure 10. The longitudinal structure function $F_L(x, Q^2)$ as obtained by H1 and by charged lepton-proton fixed target experiments. The inner error bars reflect the statistical errors, the total error bars the statistical and systematical errors, added in quadrature. The error bands are due to the experimental (inner) and model (outer) uncertainty of the calculation of F_L using the NLO QCD fit to the H1 96/97 data for $y < 0.35$ and $Q^2 \geq 3.5$ GeV^2.

calculating F_L using QCD. The QCD[16] prediction is in good agreement with the H1 estimate.

5 Deep inelastic scattering at low x

Until now we have concentrated on hard processes, in which Q^2 has been large and where QCD has shown itself to be applicable. However, the data, in particular the ZEUS "BPT" data [20], give access to very low Q^2 and x regimes, in which the strong interaction becomes very strong and perturbative QCD would be expected to break down. This kinematic region has traditionally been understood in terms of Regge theory. The study of how and where the transition between these two regimes occurs is very interesting, not only intrinsically but also because of the insight it gives us into links between the

apparently rather different processes of diffraction and deep inelastic scattering. In addition, the access given to very low values of x at these small Q^2 in principle gives sensitivity to the mechanism of QCD evolution. Given the steep rise in the parton densities as x falls, the data at the lowest x values may also be sensitive to high-density effects, such as parton recombination, sometimes known as saturation.

5.1 QCD evolution

We assume that the parton distribution functions, f, satisfy the schematic equation:

$$\frac{\partial f}{\partial \ln \mu^2} \sim \frac{\alpha_s(\mu^2)}{2\pi} \cdot (f \otimes \mathcal{P}) \tag{42}$$

where μ represents the renormalisation scale and $\mathcal{P}$ is a 'splitting function' that describes the probability of a given parton splitting into two others. This equation is known as the Dokshitzer-Gribov-Lipatov-Altarelli-Parisi (DGLAP) Equation [21–24]. There are four distinct Altarelli-Parisi (AP) splitting functions representing the 4 possible $1 \to 2$ splittings and referred to as P_{qq}, P_{gq}, P_{qg} and P_{gg}. The calculation of the splitting functions in perturbative QCD in Eq. 42 requires approximations, both in order of terms which can be taken into account as well as the most important kinematic variables. The generic form for the splitting functions can be shown to be [25]:

$$x\mathcal{P}(x, \alpha_s) = \sum_{n=0}^{\infty} \left(\frac{\alpha_s}{2\pi}\right)^n \left[\sum_{m=0}^{n} A_m^{(n)} \left\{\ln\left(\frac{1}{x}\right)\right\}^m + x\overline{\mathcal{P}}^{(n)}(x)\right] \tag{43}$$

where $\overline{\mathcal{P}}^{(n)}(x)$ are the x-finite parts of the AP splitting functions and $A_m^{(n)}$ are numerical coefficients which can in principle be calculated for each splitting function. In the axial gauge, leading $\ln Q^2$ terms arise from evolution along the parton chain that is strongly ordered in transverse momentum, i.e.

$$Q^2 \gg k_{t,n}^2 \gg k_{t,n-1}^2 \gg \ldots$$

Leading-order DGLAP evolution sums up $(\alpha_s \ln Q^2)^n$ terms, while NLO sums up $\alpha_s(\alpha_s \ln Q^2)^{n-1}$ terms, which arise when two adjacent transverse momenta become comparable, losing a factor of $\ln Q^2$.

In some kinematic regions, and in particular at low x, it must become essential to sum leading terms in $\ln 1/x$ independent of the value of $\ln Q^2$. This is done by the Balitsky-Fadin-Kuraev-Lipatov [26–29] (BFKL) equation, which governs the evolution in x at fixed Q^2. The leading-order terms in $(\alpha_s \ln 1/x)^n$ arise from strong ordering in x, i.e.

$$x \ll x_n \ll x_{n-1} \ll \ldots$$

One of the most important goals of HERA physics is the search for experimental effects that can be unambiguously attributed to BFKL evolution.

Generally, however, QCD coherence implies angular ordering. To see the implications of this it is more convenient to work with unintegrated parton density functions, $f(x, k_t^2, \mu^2)$, where μ is the scale of the probe. There are now two hard scales, k_t and complicated QCD evolution, known as the Ciafaloni, Catani, Fiorani and Marchesini [30–32] (CCFM) evolution equation. The DGLAP and BFKL equations can then be seen to be two limits of angular ordering. In the DGLAP collinear approximation, the branching angle, θ, where $\theta \sim k_t/k_l$, grows since k_t grows; while for BFKL evolution, θ grows because $k_l \propto x$ falls.

Figure 16 shows the $\ln 1/x$ - $\ln Q^2$ plane at HERA, together with schematic indications of the directions in which GLAP, BFKL and CCFM evolution is expected to be most applicable. Also indicated on the figure are schematic

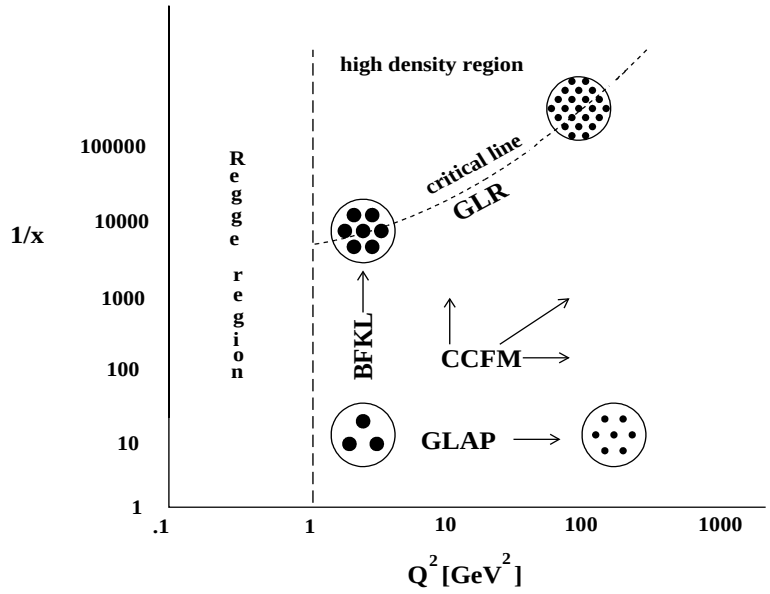

Fig. 16. Schematic diagram showing different regions of the $\ln 1/x$ and $\ln Q^2$ plane and the evolution equations expected to hold therein. The line marked 'saturation' represents the boundary between GLAP evolution and evolution governed by the GLR equation. The 'size' of partons is also indicated in differing kinematic regions.

indications of both the 'size' and density of partons in the proton in different kinematic regions.

The transverse size of the partons that can be resolved by a probe with virtuality Q^2 is proportional to $1/Q$, so that the area of the partonic 'dots' in Fig. 16 falls as Q^2 rises. For particular combinations of parton size and density, the proton will eventually become 'black' to probes, or, equivalently,

the component gluons will become so dense that they will begin to recombine. The dotted line labelled 'Critical line - GLR' refers to the boundary beyond which it is expected that such parton saturation effects will become important, i.e. the region in which partons become so densely crowded that interactions between them reduce the growth in parton density predicted by the linear GLAP and BFKL evolution equations. The parton evolution in this region can be described by the Gribov-Levin-Riskin [33,34] equation, which explicitly takes into account an absorptive term in the gluon evolution equation. Naively, it can be assumed [35] that the gluons inside the proton each occupies on average a transverse area of πQ^{-2}, so that the total transverse area occupied by gluons is proportional to the number density multiplied by this area, i.e. $\pi Q^{-2} xg(x, Q^2)$. Since the gluon density increases quickly as x falls, and the gluon 'size' increases as Q^{-1}, in the region in which both x and Q^2 are small, saturation effects ought to become important. This should occur when the size occupied by the partons becomes similar to the size of the proton:

$$xg(x, Q^2)\frac{\pi}{Q^2} = \pi R^2 \tag{44}$$

where R is the radius of the proton, (~ 1 fm ~ 5 GeV^{-1}). The measured values of $xg(x, Q^2)$ imply that saturation ought to be observable at HERA [36] at low x and Q^2, although the values of Q^2 which satisfy Eq. 44 are sufficiently small that possible non-perturbative and higher-twist effects certainly complicate the situation. Of course,

it is also possible that the assumption of homogenous gluon density is incorrect; for example, the gluon density may be larger in the close vicinity of the valence quarks, giving rise to so-called 'hot spots' [37], which could lead to saturation being observable at smaller distances and thereby larger Q^2.

5.2 Interpretation and Models

The region of low Q^2 and low x is one in which perturbative QCD meets and competes with a large variety

of other approaches, some based on QCD, others either on older paradigms such as Regge theory or essentially *ad-hoc* phenomenological models. In a previous article [38] I gave a quite detailed review of these models, and given that there have not been major developments here, I refer the reader to that for further information.

5.3 QCD fits

The extension of the kinematic range and the high-precision data on F_2 from HERA provided a substantial impetus to the determination of parton distribution functions via global fits to a wide variety of data. The major current

approaches are due to the CTEQ group [39] and Martin et al. (MRST) [40]. In general both groups fit to data from fixed target muon and neutrino deep inelastic scattering data, the HERA DIS data from HERMES, H1 and ZEUS, the W-asymmetry data from the Tevatron as well as to selected process varying from group to group such as prompt photon data from Fermilab as well as high-E_T jet production at the Tevatron. The different data sets give different sensitivity to the proton distributions, depending on the kinematic range, but together constrain them across almost the whole kinematic plane, with the possible exception of the very largest values of x, where significant uncertainties still remain [41].

The approaches of CTEQ and MRST are basically similar, although they differ both in the data sets used as well as in the fitting procedure and the technical details of the theoretical tools used, e.g. the treatment of heavy quarks in DIS. In their latest fits, CTEQ prefer to omit the prompt photon data because of the uncertainties in scale dependence and the appropriate value for the intrinsic k_T required to fit the data. Instead they use single-jet inclusive E_T distributions to constrain the gluon distribution at large x. In contrast, until their most recent publications, MRST retained the prompt photon data, giving alternative PDFs depending on the value for the prompt-photon intrinsic k_T used. Both groups parameterise the parton distributions in terms of powers of x and $(1-x)$ leading to fits with many free parameters. The MRST NLO parameterisation of the gluon is shown below as an example:

$$xg = A_g x^{-\lambda_g} (1-x)^{\eta_g} (1 + \epsilon_g \sqrt{x} + \gamma_g x) \tag{45}$$

where $A_g, \lambda_g, \eta_g, \epsilon_g$ and γ_g are free parameters in the fit.

The seminal work of Botje in producing PDFs with associated error matrices for the first time [42] has led to similar fits being produced by other groups. CTEQ [43] have produced a global fit with associated errors, while both H1 [44] and ZEUS [45] have produced their own fits using DIS data only, as discussed in Section 4.2.

These fits allow one to see very graphically the salient features of the QCD evolution that have been discussed above. For example, the ZEUS NLOQCD fit shown in Fig. 9 has already been discussed in Section 4.2. Here we saw that the strange behaviour both of the gluon vs. sea densities, as well as F_L, as a function of Q^2 showed that the normal QCD interpretation may well be breaking down at Q^2 around 1 GeV^2.

One possible reason for the problems with the interpretation of the NLO QCD fits could be the need for higher-order QCD fits i.e. next-to-next-to-leading-order (NNLO) fits. The first steps in implementing such fits have already begun; some moments of the NNLO splitting functions have been calculated [46]. Using this with other available information, van Neerven and Vogt [47,48] have produced analytical expressions for the splitting functions which represent the slowest and fastest evolution consistent with the currently

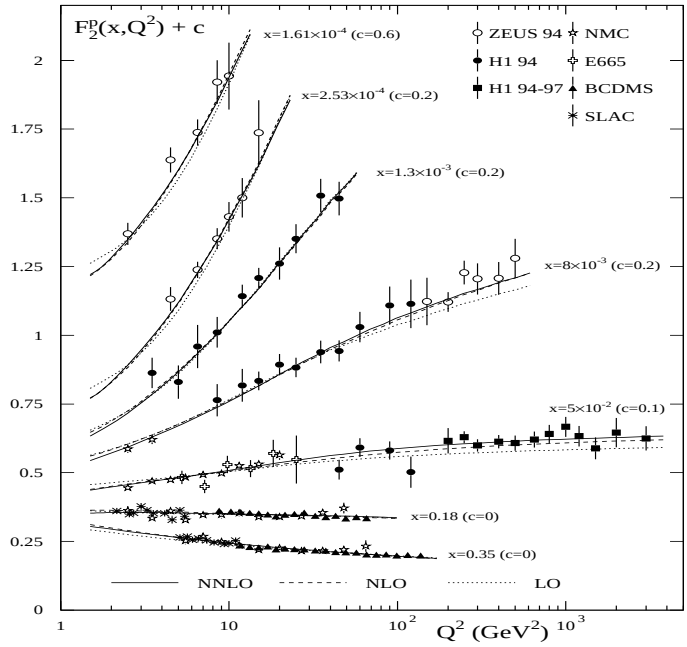

Fig. 17. The MRST 'central' NNLO fit to DIS data. The solid line shows the NNLO fit, while the NLO fit is shown by the dashed line and the LO fit by the dotted line. The data are from H1, ZEUS and the fixed target experiments and are plotted in x bins as a function of Q^2 with an additive constant added to the data of each x bin to improve visibility.

available information. The MRST group has recently used this information to investigate NNLO fits to the available data [49]. Such an analysis requires some changes to the parameterisations used, so that for example the NLO parameterisation of the gluon of Eq. 45 becomes:

$$xg(x,Q_0^2) \;=\; A_g\, x^{-\lambda_g}\,(1-x)^{\eta_g}\,(1+\varepsilon_g\sqrt{x}+\gamma_g x) \;-\; A'_g\, x^{-\lambda'_g}\,(1-x)^{\eta'_g}, \quad (46)$$

primarily in order to facilitate a negative gluon density at low x and low Q^2, which, as we have seen, is preferred by the fits, even at NLO. The results of the 'central' fit, between the extremes of the van Neerven-Vogt parameterisation, is shown in Fig. 17.

There are also changes of the LO and NLO fits with respect to earlier publications, in as much as MRST now follow CTEQ in using the Tevatron high-E_T data rather than the prompt-photon data, and HERA F_2 data has been included in the fit. There is a marked improvement in the quality of

the fit in the progression LO → NLO → NNLO, in particular in terms of the NMC data. The size of higher-twist contributions at low x also decreases, so that at NNLO is it essentially negligible. The effect of going to NNLO on the PDFs themselves is highly non-trivial. This is illustrated in Fig. 18, where the quite major changes in F_L, particularly at low x, are evident. There is also a large variation depending on the choices made in the parameter space allowed by the partial NNLO *ansatz*. Indeed, the GLAP approach is not convergent for $Q^2 < 5$ GeV^2, which may well be due to the neglect of important $\ln 1/x$ contributions. However, the instability seen at low Q^2 soon vanishes at higher Q^2.

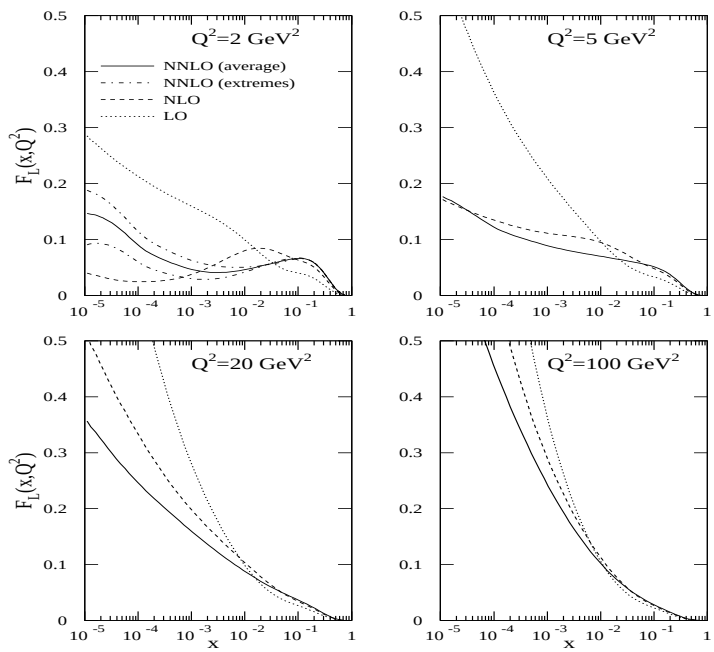

Fig. 18. The F_L structure function from the MRST fits, taking into account part of the NNLO corrections in four bins of Q^2 as a function of x. The solid line shows the 'average' of the parameter space available to choose the NNLO parameters, while the dashed-dotted lines show the two extreme possibilities. The NLO fit is indicated by the dashed line while the LO fit is indicated by the dotted line.

Thorne has investigated the question of incorporating $\ln 1/x$ terms in the splitting functions by incorporating the solution of the NLO BFKL kernel using a running coupling constant [50,51]. The inclusion of the BFKL terms

does indeed give an improved fit compared to the 'central' NNLO fit, particularly at the lowest Q^2 and x. This may be one of the first unambiguous indications of the importance of BFKL evolution.

5.4 Data in the transition region

The approximate position of the transition between data that can be described by pertrubative QCD evolution and that which require the Regge approach can be seen in Fig. 19.

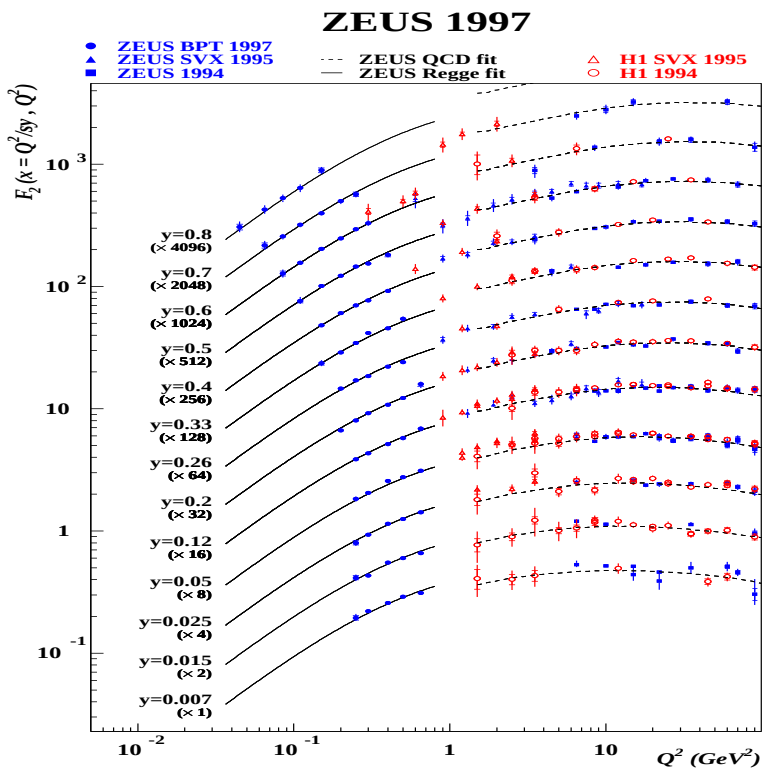

Fig. 19. ZEUS BPT data on F_2 in bins of y as a function of Q^2. Also shown are earlier ZEUS data as well as data from H1. The solid line shows the results of the ZEUS Regge fit to the form of Eq. 47, while the dotted line shows the result of the ZEUS NLO QCD fit.

For $Q^2 \gtrsim 1$ GeV^2, the data are roughly independent of Q^2, whereas at lower Q^2 they fall rapidly, approaching the Q^{-2} dependence that would be expected in the limit $Q^2 \to 0$ from conservation of the electromagnetic current. Although QCD gives a good fit to the data down to $Q^2 \sim 1$ GeV^2,

below that it is necessary to use a Regge-based fit of the form

$$F_2(x,Q^2) = \left(\frac{Q^2}{4\pi^2\alpha}\right)\left(\frac{M_0^2}{M_0^2+Q^2}\right)\left(A_{\mathbb{R}}\left(\frac{Q^2}{x}\right)^{\alpha_{\mathbb{R}}-1} + A_{\mathbb{P}}\left(\frac{Q^2}{x}\right)^{\alpha_{\mathbb{P}}-1}\right), \tag{47}$$

where $A_{\mathbb{R}}, A_{\mathbb{P}}$ and M_0 are constants and $\alpha_{\mathbb{R}}$ and $\alpha_{\mathbb{P}}$ are the Reggeon and Pomeron intercepts, respectively. Regge theory is expected to apply at asymptotic energies. The appropriate energy here is W, the centre-of-mass energy of the virtual photon-proton system, given by Eq. 4. Since, at low x, $W^2 \sim 1/x$, it would be expected that Regge fits would be applicable at very low x and Q^2.

The complete ZEUS data over six orders of magnitude in x and Q^2 are shown in x bins as a function of $\ln Q^2$ in Fig. 20, together with fixed target data from NMC and E665, which extends the range in the direction of medium x and Q^2.

The availability of this very wide range of precise data makes possible qualitatively new investigations of models that describe F_2. Since the logarithmic derivative of F_2 is directly proportional to the gluon density in leading-order QCD, which in turn is the dominant parton density at small x, its behaviour as a function of both x and Q^2 is important. The solid curves on the figure correspond to fits to a polynomial in $\ln Q^2$ of the form

$$F_2 = A(x) + B(x)\left(\log_{10} Q^2\right) + C(x)\left(\log_{10} Q^2\right)^2, \tag{48}$$

which gives a good fit to the data through the entire kinematic range. The dotted lines on Fig. 20 are lines of constant W. The curious 'bulging' shape of these contours in the small-x region immediately implies that something interesting is going on there. Indeed, simple inspection of Fig. 20 shows that the slope of F_2 at constant W begins flat in the scaling region, increases markedly as the gluon grows and drives the evolution of F_2 and then flattens off again at the lowest x.

Figure 21 shows the logarithmic derivative evaluated at (x, Q^2) points along the contours of fixed W shown on Fig. 20 according to the derivative of Eq. 48, *viz.*:

$$\frac{\partial F_2}{\partial \log_{10} Q^2} = B(x) + 2C(x)\log_{10} Q^2, \tag{49}$$

where the data are plotted separately as functions of $\ln Q^2$ and $\ln x$. The turn-over in the derivatives in all W bins is marked. Within the framework of pQCD, the interpretation of such an effect is that the growth of the gluon density at low x is tamed as Q^2 and x fall. This behaviour can also be seen more clearly in Fig. 22, which shows a three-dimensional plot of the derivatives as a function of both $\ln x$ and $\ln Q^2$, obtained from a parameterisation of the DIS data.

Such an effect is by no means necessarily an indication of deviations from the standard DGLAP evolution. It can be seen from Fig. 22 that, for example,

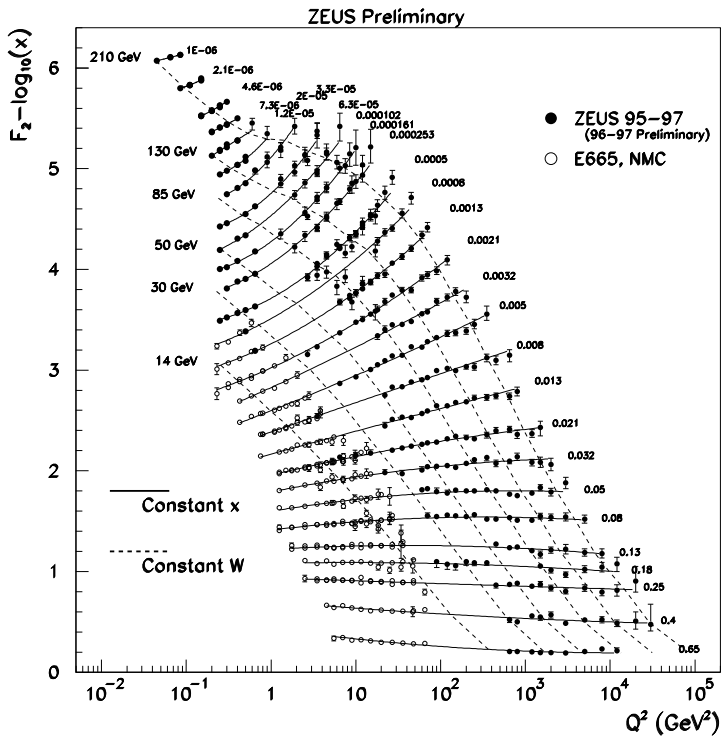

Fig. 20. Compilation of ZEUS F_2 data in x bins as a function of Q^2. Each x bin is shifted by an additive constant for ease of visibility. Data from NMC and E665 are also shown. The dotted lines show lines of constant W, while the solid lines are fits to the form of Eq. 48.

no turnover effect occurs in bins of constant Q^2. Nevertheless, the features of Figs. 21 and 22 can be explained as a natural consequence of parton saturation or shadowing. These effects can be naturally discussed in "dipole models" [38], which often explicitly take into account parton-saturation effects. In such models, the "standard" picture of deep inelastic scattering in the infinite-momentum frame of the proton is replaced by an equivalent picture produced by a Lorentz boost into the proton rest frame. In this frame, the virtual photon undergoes

time dilation and develops structure far upstream of the interaction with the proton. The dominant configurations of this structure are $q\overline{q}$ and $q\overline{q}g$ Fock states, which interact with the proton as a colour dipole. The higher the Q^2 of the interaction, the smaller the transverse size of the dipole. For small x, the deep inelastic process can be considered semi-classically as the coherent

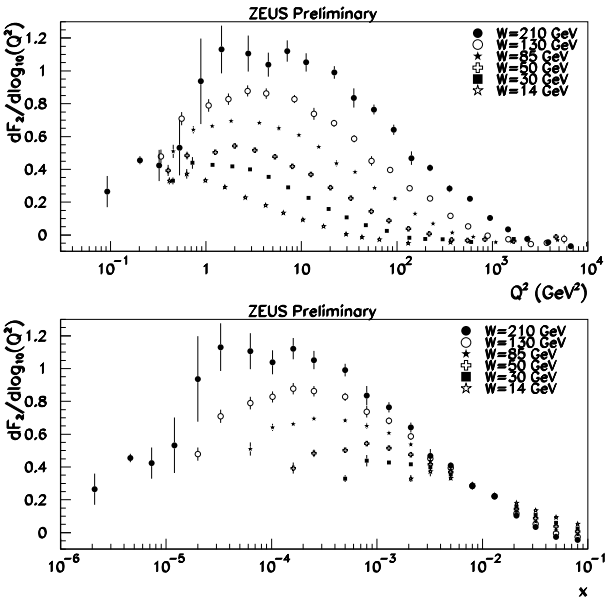

Fig. 21. The logarithmic derivative of the ZEUS F_2 data in six bins of W, plotted as a function of Q^2 and x.

interaction of the dipole with the stationary colour field of the proton a long time after the formation of the dipole. As an example, the model of Golec-Biernat and Wüsthoff (GBW) [52,53] is shown in Fig. 23, together with the results of the ZEUS NLOQCD fit.

It can be seen that the GBW model reproduces the basic features of the logarithmic derivative plot reasonably well. However, so does the ZEUS NLOQCD fit, so that no firm conclusion can be drawn on the existence or otherwise of saturation effects.

6 Diffraction

Diffractive DIS is that subset characterised by a hard interaction between the proton and the exchanged virtual photon that nevertheless leaves the proton intact. Such interactions are normally thought of in Regge theory as proceeding via the exchange of a colourless particle with the quantum numbers of the vacuum, known as the Pomeron. The Pomeron under some circumstances can be considered to develop its own partonic structure, analogous to the proton, which can be parameterised using diffractive DIS data.

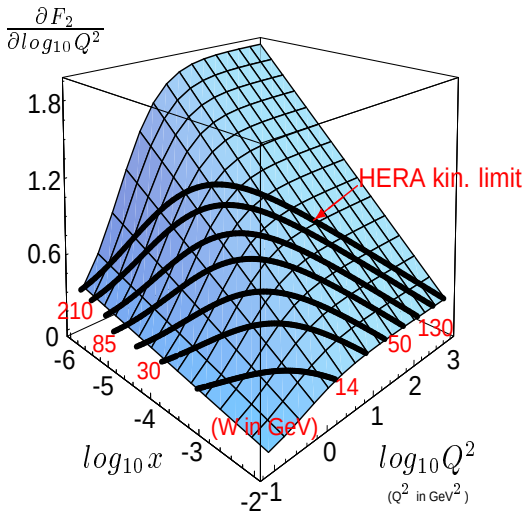

Fig. 22. The logarithmic derivative of the ZEUS F_2 data plotted as a surface in three dimensions versus both Q^2 and x. The curves show lines of constant W.

One of the most attractive features of dipole models such as that of GBW discussed in the previous section is the rather natural way in which they can lead to a unified description of diffraction and deep inelastic scattering. The QCD interpretation of the Pomeron is that it is equivalent to the exchange of two gluons in a colour-singlet state. In this picture, therefore, diffraction can be considered as a subset of fully inclusive DIS, which sums over all possible exchanges between the dipole and the proton, dominantly one- and two-gluon exchange in a colour octet, in contrast to the colour-singlet exchange that dominates inclusive DIS. This deep connection between these two processes leads to non-trivial predictions which do indeed seem to be at least qualitatively in agreement with the data. This is illustrated in Fig. 24. This figure is surprising for several reasons. It demonstrates that the diffractive cross section has the same W dependence as the total cross section. To the extent to which the diffractive cross section can be related to the elastic cross section, one would have expected from the Optical Theorem that the ratio would have a power-law dependence on W, as indeed would also be expected from Regge theory via the exchange of a Pomeron. A strong W ($\sim 1/x$) dependence is also expected in QCD models, since the total cross section is dominated by single-gluon exchange, whereas diffraction is dominated by two-gluon exchange. The other surprise is the fact that the GBW model gives a rather good qualitative representation of the data.

ZEUS has also investigated the behaviour of this ratio as $Q^2 \to 0$ [54]. Figure 25 shows the diffractive structure function, $x_{\mathbb{P}} F_2^{D(3)}$ (the analogue to F_2, integrated over t) multiplied by $x_{\mathbb{P}}$, the fraction of the protons momen-

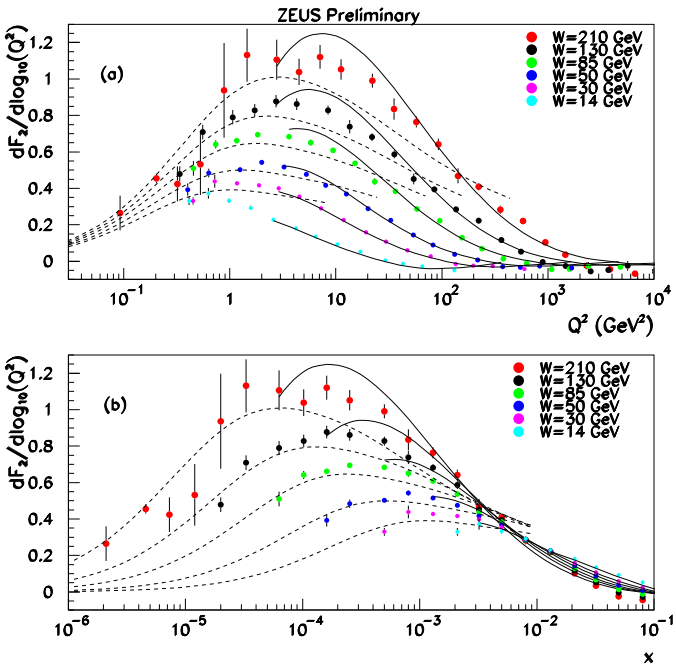

Fig. 23. The logarithmic derivatives of the ZEUS F_2 data as shown in Fig. 21. The dotted curves show the predictions of the BGW model for the five highest W bins; since these predictions do not include QCD evolution effects, they should become progressively less accurate as Q^2 increases. The solid curves show the predictions of the ZEUS NLO QCD fit for all W bins; they are only shown down to $Q^2 \sim 3$ GeV^2.

tum carried by the Pomeron, as a function of Q^2 in various bins of W and in two bins of M_X, the mass of the hadronic system other than the proton. The $F_2^{D(3}$ data points are determined using two methods, one of which requires the observation of a large rapidity gap in the proton-beam direction, while the other uses the ZEUS Leading Proton Spectrometer (LPS) [55]. This device is an array of six stations of silicon-strip detectors placed in Roman pots downstream of the interaction point in the proton beam direction. It uses the HERA beam elements to form a magnetic spectrometer to analyse the leading proton from diffractive interactions. Although its acceptance is of necessity small, it avoids the low-mass proton dissociative background endemic with other forms of identifying diffractive interactions. The similarity of Fig. 25 to Fig. 19 is striking, again illustrating the Q^{-2} falloff enforced by electromagnetic current conservation.

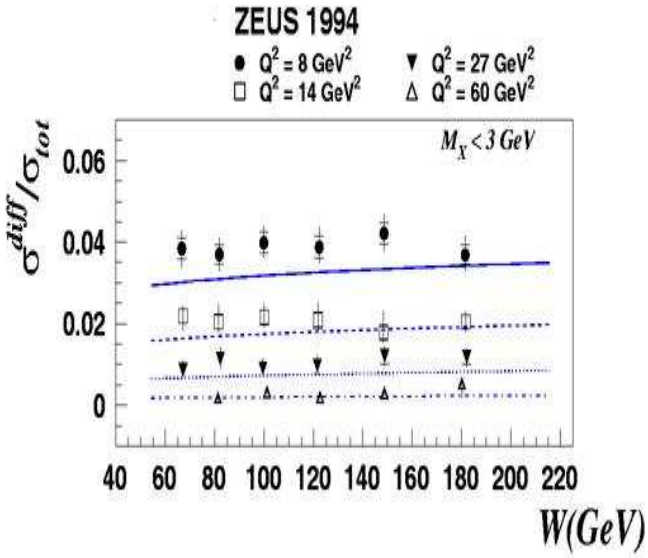

Fig. 24. The ratio of the diffractive to total cross section in four Q^2 bins as a function of W. The curves show the predictions from the Golec-Biernat & Wusthoff model.

6.1 Vector meson production

The exclusive production of vector mesons is both a very simple laboratory to study many aspects of diffraction as well as a process in which dipole models are likely to be particularly appropriate. Figure 26 shows the photoproduction cross sections for a variety of vector mesons as a function of W, as well as the total cross section. The relatively slow rise of the total cross section with Q^2 is indicative of the dominance of soft processes. The J/ψ cross section clearly has a much steeper rise with Q^2. This is more clearly seen in Fig. 27, where the cross section for several different Q^2 is shown as a function of W. It would appear that the mass of the J/ψ is sufficiently large that it gives rise to a hard scale even at $Q^2 \sim 0$.

In contrast, the mass of the ρ is small and quite large values of Q^2 need to be reached before the W dependence rises to the values associated with hard processes. This can be seen in Fig. 28, which shows the values of the fit to a power law in W as a function of Q^2. An appropriately hard scale seems to pertain for $Q^2 > 5$.

This behaviour, in which either Q^2 or the mass can act as a hard scale, leads to the obvious question of whether a combination of these two quantities can also give a hard scale. Figure 28 shows the data on ρ, ϕ and J/ψ production from H1 and ZEUS plotted against $Q^2 + M^2$. There is indeed a tendency for the data for all the vector mesons to lie on a universal curve.

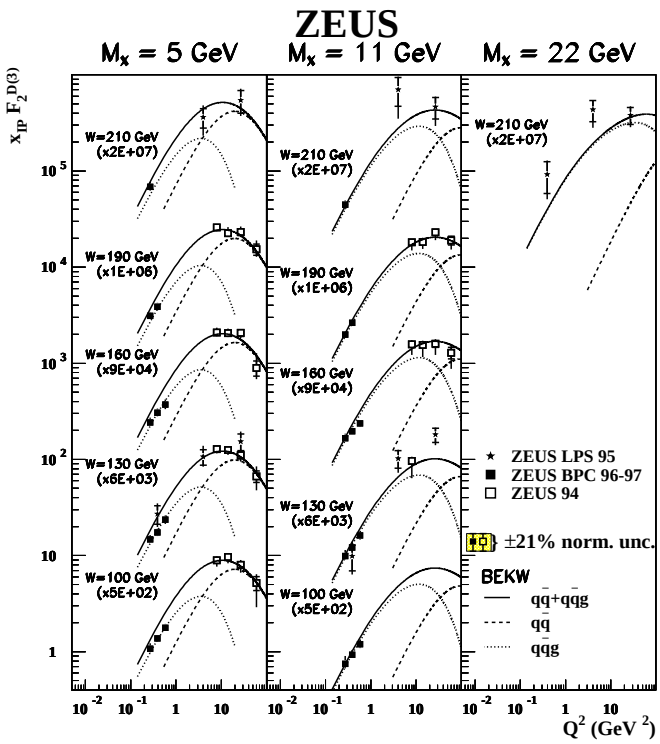

Fig. 25. $x_{\mathbb{P}} F_2^{D(3)}$ in bins of W and M_X as a function of Q^2. The curves refer to the model of Bartels et al. [56]

However, other more detailed comparisons [57] show that some differences do remain between the different species even when plotted against $Q^2 + M^2$.

To the extent that we can model diffraction by the exchange of a colourless two-gluon state, we would expect a difference between the W dependence of vector meson production and inclusive DIS. This is illustrated in Fig. 29 shows the values of fits to the W-dependence of the inclusive DIS and vector-meson cross sections against Q^2 and $Q^2 + M^2$, respectively. For $Q^2 + M^2$ greater than about 5 GeV^2, the value of δ is indeed about twice that at the same value of Q^2 in inclusive DIS, as would be expected in the simple picture of two-gluon exchange.

Provided that we have a scale sufficiently hard that pQCD is applicable, we can also use vector meson production to probe the gluon density in the proton. Since the cross section is proportional to the gluon density squared, such a determination should in principle be much more sensitive to the gluon density than, for example, scaling violations in deep inelastic scattering. This is illustrated in Fig. 30, which shows ZEUS and H1 data for J/ψ photoproduction as a function of W. We have seen already that the J/ψ mass is

PHOTPRODUCTION OF VECTOR MESONS

36 B. Foster

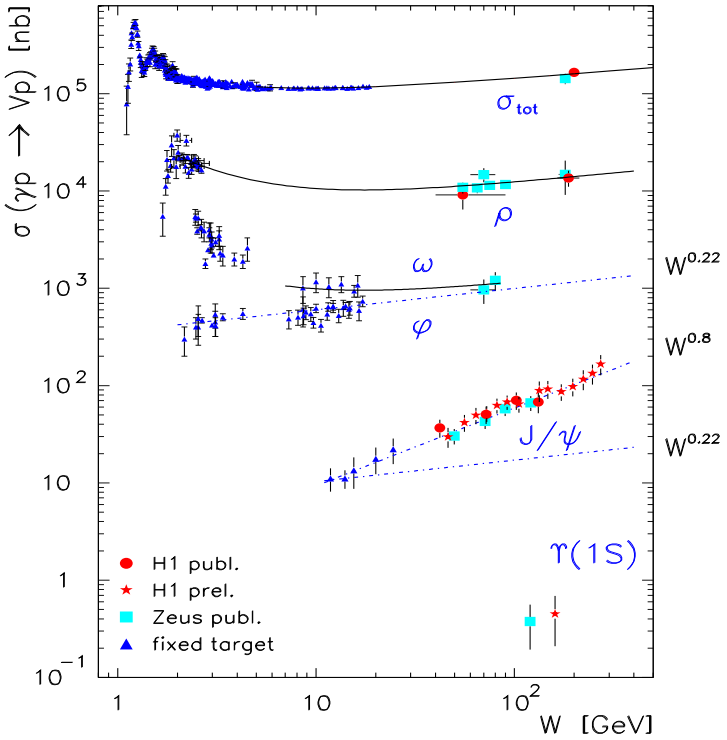

Fig. 26. The total photoproduction cross section together with the photoproduction cross sections for a variety of vector mesons as a function of W from H1, ZEUS and several fixed-target experiments. The dotted lines show W to the indicated powers.

J/ψ rises like $W^{0.8}$! (i.e. twice Γ_2 at 10 GeV)

sufficiently large to guarantee that pQCD is applicable even in photoproduction. The quality of the data is sufficiently high that it is in principle sensitive to the gluon density. Unfortunately, the wave-function of the J/ψ must be modelled, which leads to substantial uncertainty in the model predictions, so that this data has not as yet been used in global fits to constrain the gluon density. The good agreement between at least some version of the models and the data, as shown in Fig. 30, does however indicate that the gluon determined in the global fits to DIS data is indeed also able to explain the dynamics of this completely different diffractive process.

Finally, it is interesting to investigate whether t can also provide a hard scale for pQCD. ZEUS has precise data out to $-t \sim 12$ GeV^2 for ρ production and also to beyond 6 GeV^2 for ϕ and J/ψ. The ratio of the cross sections for ϕ and ρ starts somewhat below the $SU(4)$ expectation but reaches it quite quickly, by $-t \sim 3-4$ GeV^2. In contrast, the J/ψ ratio remains below the $SU(4)$ prediction for much longer, hardly reaching it even for $-t \sim 6$ GeV^2.

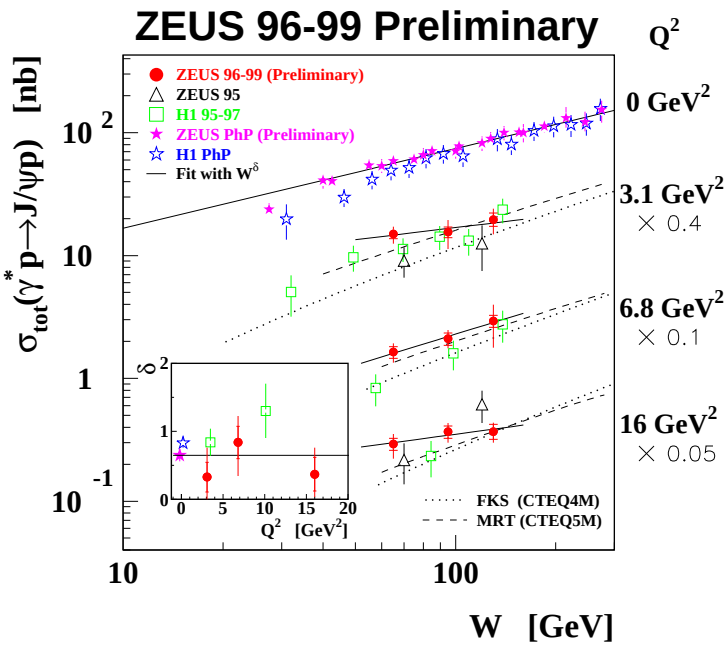

Fig. 27. The ZEUS and H1 J/ψ cross section for several bins of Q^2 as a function of W. The dotted lines show the predictions of the model of Frankfurt, Koepf and Strikman [58], the dashed lines show the predictions of Martin, Ryskin and Teubner [59] and the solid lines show fits to the form of W^δ. The inset shows the δ obtained from these fits as a function of Q^2.

Figure 31 shows the ZEUS data for all three vector mesons as a function of $-t$ compared to a two-gluon exchange model and to a model in which a BFKL gluon ladder is exchanged [60]. It can be seen that the two-gluon model completely fails to reproduce the data both in magnitude and in shape, whereas the BFKL model, which has been fit to the ZEUS data, gives an excellent fit for all three mesons. Although some of the model assumptions, such as a fixed α_s and a δ-function wave-function for the light vector mesons, are somewhat questionable, the fact that this BFKL model fits the data whereas conventional pQCD fails is very striking. It can thus be concluded that t does form an appropriate hard scale for pQCD calculations. However, the ratios of ZEUS vector-meson cross sections behave differently as a function of t compared to Q^2, so that either these ratios are different at asymptotic values of the two variables, or t and Q^2 are not equivalent hard scales.

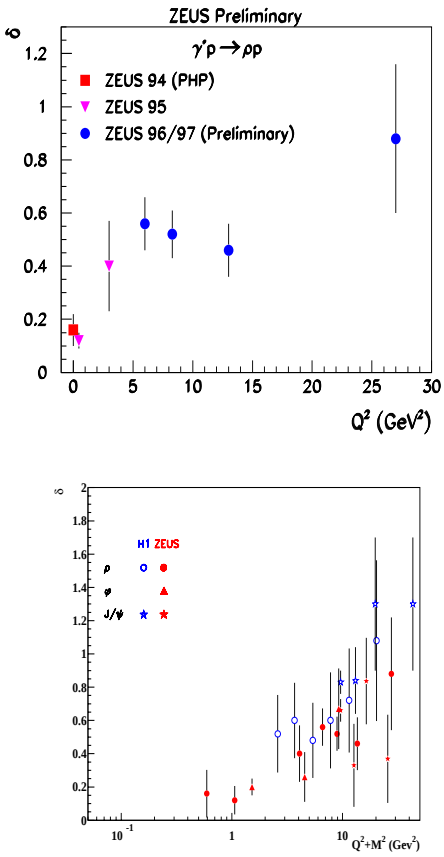

Fig. 28. a)Results of a fit to the ZEUS ρ data of the form W^{δ}. The value of the exponent is plotted as a function of Q^2. b) The exponent obtained from fits of the form W^{δ} to the vector meson data from ZEUS and H1. The value of the exponent δ is plotted against $Q^2 + M^2$.

6.2 Deeply virtual Compton scattering

Deeply virtual Compton scattering (DVCS) is an interesting process in that it is the simplest possible non-elastic diffractive process. It consists of diffractive scattering of the virtual photon from the proton, putting the virtual photon onto mass shell so that the final state consists of the initial proton and positron plus a photon. As such, no fragmentation or hadronic wavefunctions complicate the process. The Bethe-Heitler QED process also leads to the same final state, which is both a blessing and a curse. The curse is that is necessary to separate the two processes; the blessing is that the fact of identical final states leads to interference. Since the amplitude and phase

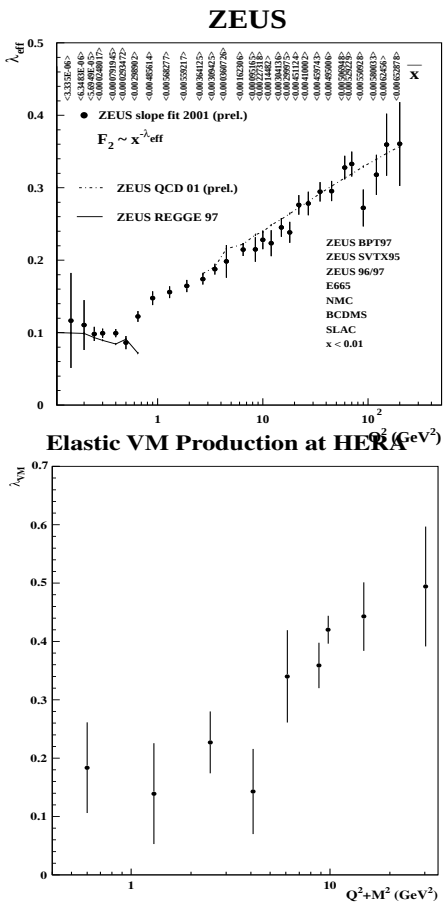

Fig. 29. a) Values of the exponent in fits of the form W^δ to the W dependence of the inclusive DIS total cross section, as a function of Q^2. b) Values of the exponent in fits of the form W^δ to the W dependence of the cross section for a variety of vector mesons, as a function of $Q^2 + M^2$.

of the QED process is calculable, in principle this opens the door to the determination of the unknown QCD amplitude that governs DVCS. However, we are still some considerable distance from this goal.

Given that a virtual photon participates in the collision with the parton in the proton and that it emerges on mass shell, it is clear that the scattered parton that must be re-integrated into the final-state proton must undergo a change in its four-momentum corresponding to a change in its x value. Thus the DVCS process is sensitive to the so-called "skewed parton distributions inside the proton, which can be thought of as the cross-correlation function

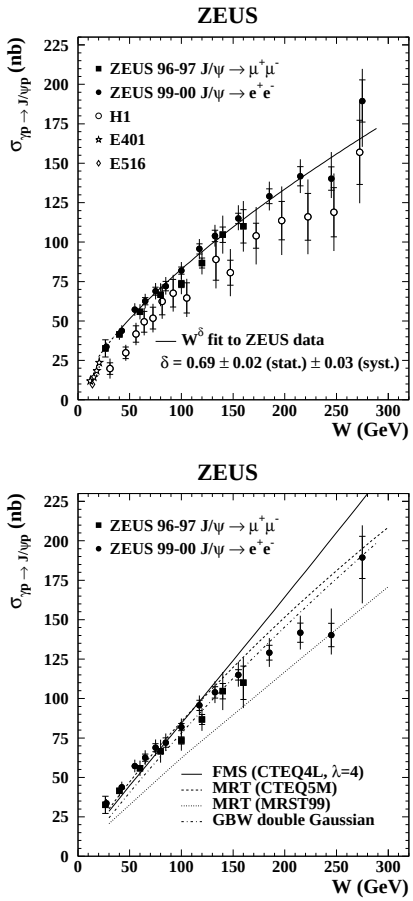

Fig. 30. a) The ZEUS and H1 data on J/ψ photoproduction, together with the data from two fixed target experiments as a function of W. The curve shows a fit to the form W^{δ}. b) The ZEUS data together with curves showing the predictions using the stated gluon pdfs from the models of Frankfurt, McDermott and Strikman [65] and Martin, Ryskin and Teubner [59].

between partons of fractional momentum x_1 and x_2. Thus much unique information can be obtained by studying these processes.

The DVCS process was first seen at HERA by ZEUS [61]. The H1 collaboration has published results on the observation of this process and the first measurement of the cross section [62]. The background from the Bethe-Heitler process can be subtracted by utilising the kinematic characteristics of the two processes. In DVCS, the photon is normally produced at a large angle to the incident beam directions and the positron at a small angle, whereas, for the Bethe-Heitler process, the reverse is the case. The sum of Monte Carlo

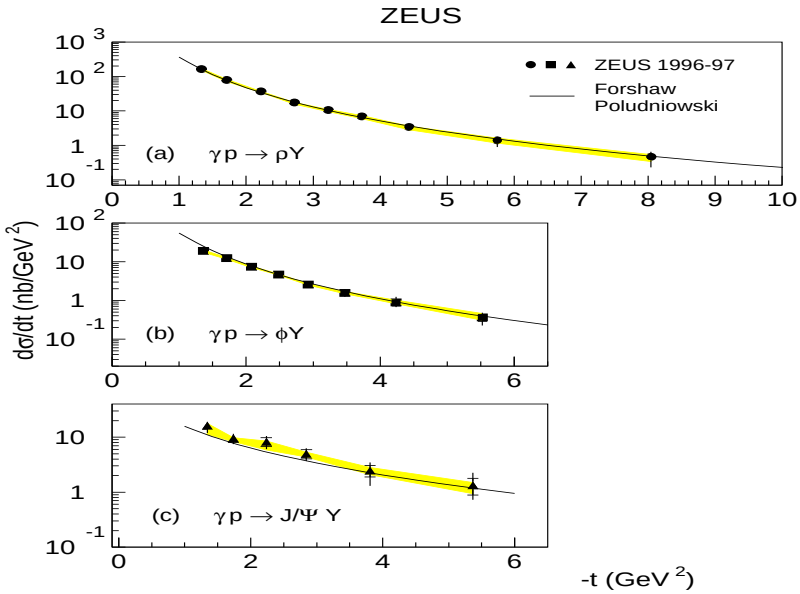

Fig. 31. The ZEUS data on vector-meson production at high $-t$. The curve shows a fit to a BFKL-model by Forshaw and Poludniowski.

Figure 8: The measured differential cross sections $d\sigma_{\gamma p \to VY}/dt$ (symbols) for (a) ρ, (b) ϕ, (c) J/Ψ production in the range $80 < W < 120\,GeV$ and $0.01 < \hat{x} < 1$. The solid curves show a pQCD calculation [16]. The inner bars indicate the statistical uncertainty and the outer bars represent the statistical and systematic uncertainties added in quadrature. The shaded bands represent the size of the uncertainties in the pQCD calculation due to the description of the hadronic structure.

generators describing the two processes gives a good description of the kinematic quantities of the data, giving confidence that the DVCS cross section can be extracted. The H1 and ZEUS cross sections are shown in Fig. 32. It can be seen that the cross sections are completely dominated by statistical errors and that both collaborations find good agreement with theoretical models, notably that of Frankfurt, Freund and Strikman [63] and Donnachie and Dosch [64]. As more data is collected, the possibility of using this process to determine skewed parton distributions will make it a fruitful area of study at HERA II.

There are many more areas of diffraction, in particular the diffractive structure functions, which I have not been able to cover. The study of diffraction has turned out to be one of the most exciting and rich areas of HERA physics. It will continue at HERA II and will hopefully allow us to make progress in our understanding of soft interactions and the related, and fundamental, question of understanding confinement in QCD.

7 Heavy quark production

We have already touched upon the production of charm quarks at HERA in the discussion of the F_2^c in Section 4.4. In fact, copious amounts of charm are produced in photoproduction at HERA, so that for many channels, HERA is

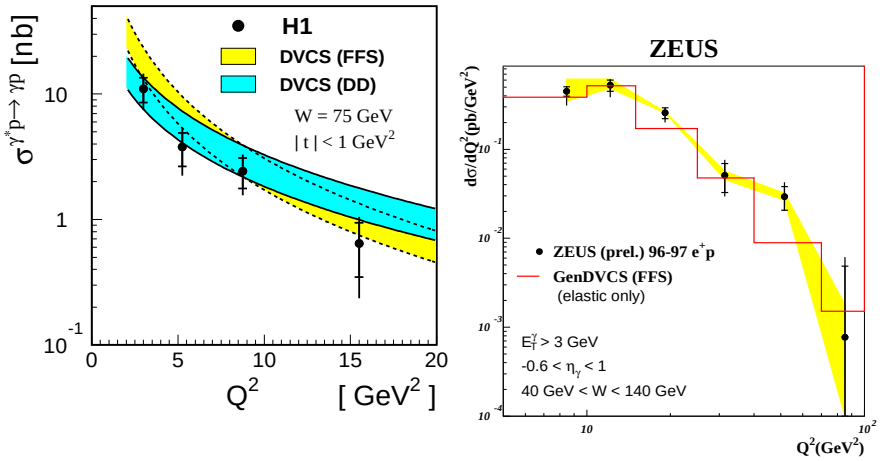

Fig. 32. a) The cross section for deeply virtual Compton scattering as a function of Q^2 as measured by the H1 collaboration. The dotted area corresponds to the prediction of Frankfurt, Freund and Strikman, while the solid area is the prediction of Donnachie and Dosch. b) The DVCS cross section as measured by ZEUS. The curve shows the prediction for the elastic process by Frankfurt, Freund and Strikman.

a "charm factory. The ZEUS collaboration has made several contributions to charm spectroscopy results: as an example, Fig. 33 shows the $D^*\pi$ spectrum from 110 pb^{-1} of data. A rather complex set of structures can be observed between 2.4 and 2.5 GeV, some of which correspond to known resonances and some of which do not. Work continues to understand this complex area; the sensitivity of ZEUS in this sort of investigation is similar to that of the LEP experiments and CLEO.

Both H1 and ZEUS have observed beauty production in photoproduction; H1 has also published a cross section in DIS. The identification of the b signal is based on the use of high-transverse-momentum leptons for ZEUS; H1 also use tracks with large impact parameter as measured in their silicon vertex detector. The results as a function of Q^2 are shown in Fig. 34. It can be seen that the QCD predictions are substantially below the data for all Q^2, thus joining a pattern also seen in proton-antiproton and photon-photon collisions. The tendency for pQCD to fail to predict B cross sections, which naively would be thought to be an area in which it should work well, is becoming increasingly interesting. The advent of HERA II will make an enormous difference to the precision of this type of measurement and should allow a stringent test of the theory of heavy-quark production.

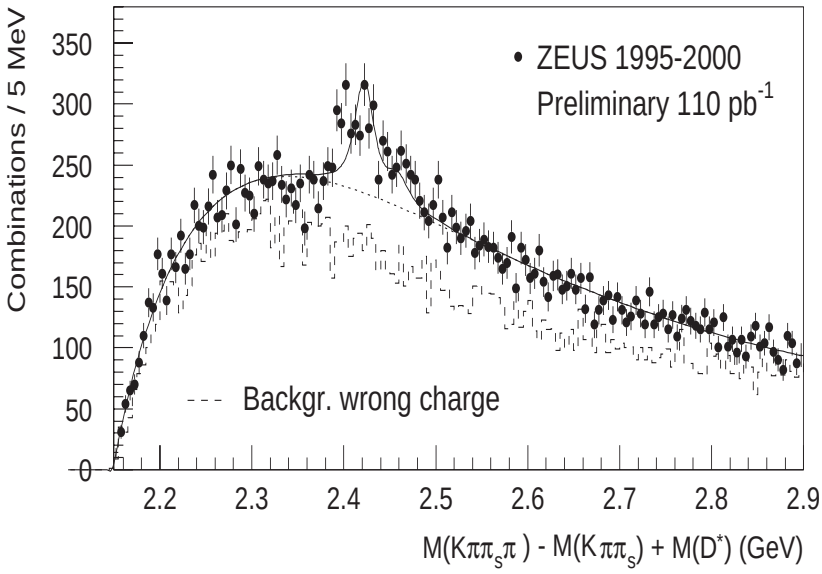

Fig. 33. The $D^*\pi$ spectrum from ZEUS, where the D^* decays via $D\pi$ and the D via $K\pi$. To improve the accuracy of the reconstruction, the effective mass of the $K\pi\pi\pi$ system minus the effective mass of the $K\pi\pi$ system that forms the D^* plus the D^* mass is plotted. The curves show a polynomial background plus Gaussians for the known D_1^0 resonance at 2.420 GeV and the D_2^* at 2.460 GeV. Another structure at just above 2.4 GeV also seems to be visible.

8 High-Q^2 phenomena

HERA provides an unique opportunity to study the electroweak interaction at Q^2 sufficiently high that the charged and neutral currents are of similar strength. Figure 35 shows the differential cross-sections for the charged and neutral currents as a function of Q^2 from H1 and ZEUS. It can be seen that, for e^-p interactions, these two processes become of equal strength at $Q^2 \sim M_Z^2 \sim 10^4$ GeV^2. For e^+p interactions, the charged current cross-section approaches the neutral current cross-section, but remains below it. The features of this plot can be explained by inspection of Eq. 26, together with Eqs. 50 and 51 below:

$$\left.\frac{d^2\sigma}{dxdQ^2}\right|_{e^-}^{CC} = \frac{G_F^2}{2\pi}\left(\frac{M_W^2}{M_W^2+Q^2}\right)^2 \cdot 2x\{u(x)+c(x)+(1-y)^2(\overline{d}(x)+\overline{s}(x))\} \tag{50}$$

$$\left.\frac{d^2\sigma}{dxdQ^2}\right|_{e^+}^{CC} = \frac{G_F^2}{2\pi}\left(\frac{M_W^2}{M_W^2+Q^2}\right)^2 \cdot$$

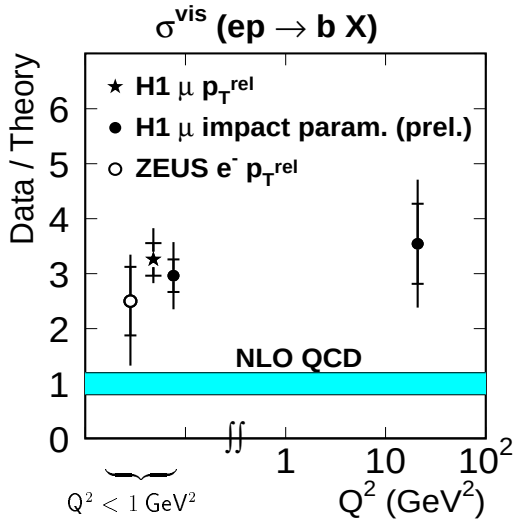

Fig. 34. The ratio of the measured cross section and the theoretical prediction, plotted against Q^2, from H1 on beauty production in photoproduction and DIS and from ZEUS in photoproduction,. The band shows the uncertainty on the predictions of perturbative QCD.

$$2x\{\overline{u}(x) + \overline{c}(x) + (1-y)^2(d(x) + s(x))\} \tag{51}$$

For the charged current case, the smaller size of the e^+p cross-section compared to e^-p is related to the fact that, at high Q^2, Eq. 3 implies that both $x, y \to 1$. There are two main contributory factors to the cross-section difference that flow from this. First, there are twice as many u valence quarks inside the proton that can couple to W^- as d quarks that can couple to W^+. Secondly, the $(1-y)^2$ terms in Eqs. 50 and 51, which arise from the $V-A$ helicity structure of the charged weak current, imply that the valence-quark contribution, which is dominant at high Q^2, is suppressed for the positron case but not for electrons.

The difference between the electron and positron neutral current cross sections shown in Eq. 26 allows the determination of the parity-violating structure function xF_3 by taking the difference of the cross sections. The results [66] are shown in Fig. 36. Since its determination requires the subtraction of two quantities that are almost equal, it is dominated by statistical uncertainties, which are in turn dominated by the fact that the electron data sample that has so far been obtained at HERA is much smaller than that for positrons.

The high-Q^2 regime is also interesting since possible new states from electron-quark fusion (e.g. leptoquarks) have masses given by $M^2 \sim sx$ and since the sensitivity to the effects of new currents is maximised. An example of the sensitivity that can be obtained at HERA is shown in Fig. 37, which shows

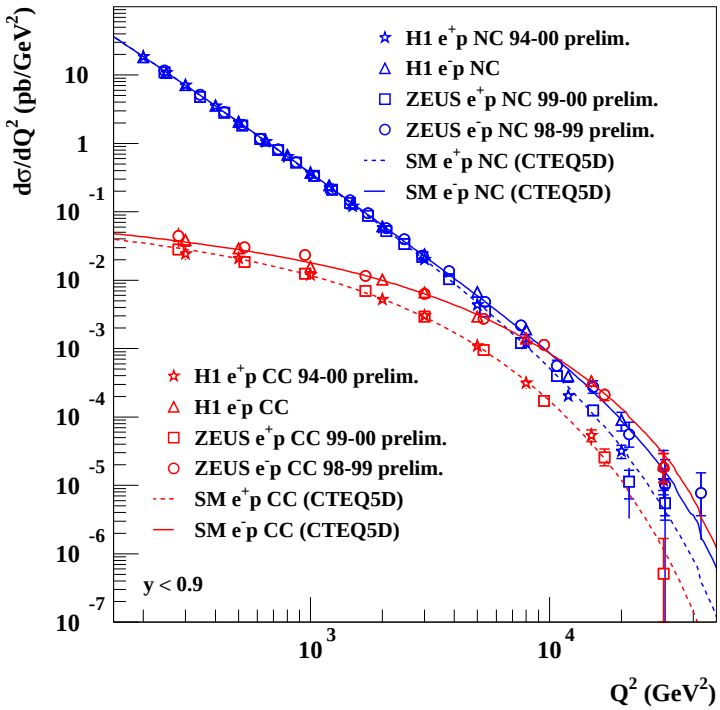

Fig. 35. Charged and neutral current differential cross sections for $e^{\pm}$ scattering as a function of Q^2 from H1 and ZEUS.

the mass against coupling limits for two varieties of scalar leptoquark. Both H1 and ZEUS have comparable limits for a whole range of such states with differing quantum numbers. It can be seen from Fig. 37, and it is generally the case, that for some states, in particular in R-parity-violating supersymmetry models or leptoquarks, HERA has higher sensitivity than either LEP or the Tevatron.

Limits on excited leptons and quarks have also been obtained by ZEUS and H1, which extend the limits from the LEP experiments considerably beyond the LEP II centre-of-mass energy.

As well as stringent limits on new phenomena, the HERA data also show intriguing features which may be signatures for new physics. The H1 collaboration has observed a class of events that have isolated charged leptons with large missing transverse momentum. Figure 38 shows the distribution of the transverse momentum of the hadronic system, p_T^X, against its transverse mass, separately for electrons (or positrons) and muons in such events. Also

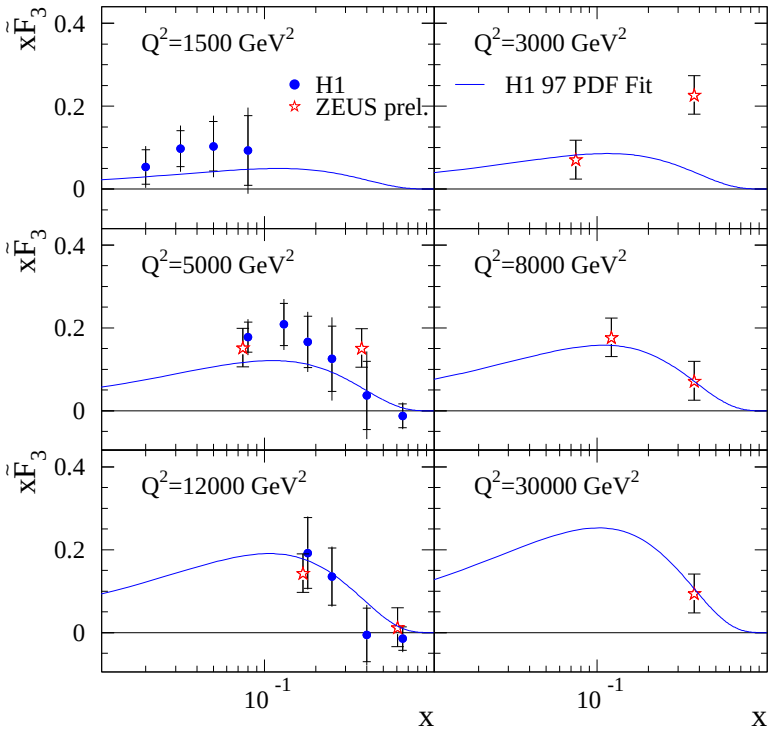

Fig. 36. The xF_3 structure function as determined by H1 and ZEUS as a function of x in six bins of Q^2.

shown are the expectations from the Standard Model background, which is dominated by single W production.

It can be seen that the distribution of the events is rather different to the Standard Model expectation. Furthermore, for the transverse mass of the hadronic system greater than 25 GeV, H1 sees four electron and six muon events, compared to Standard Model expectations of 1.3 and 1.5 events, respectively. Unfortunately, this exciting observation is not confirmed by ZEUS, which, for the same cut in p_T^X, sees one event in each category compared to the Standard Model expectation of 1.1 and 1.3, respectively. Intensive discussions between the two experiments have not revealed any reason why H1 might artificially produce such an excess nor why ZEUS should not observe it. It would therefore seem that there must be an unlikely fluctuation: either the H1 observation is an upward fluctuation from the Standard Model, or ZEUS has suffered a downward fluctuation from a signal for new physics. More data from HERA II will be required to resolve this puzzle.

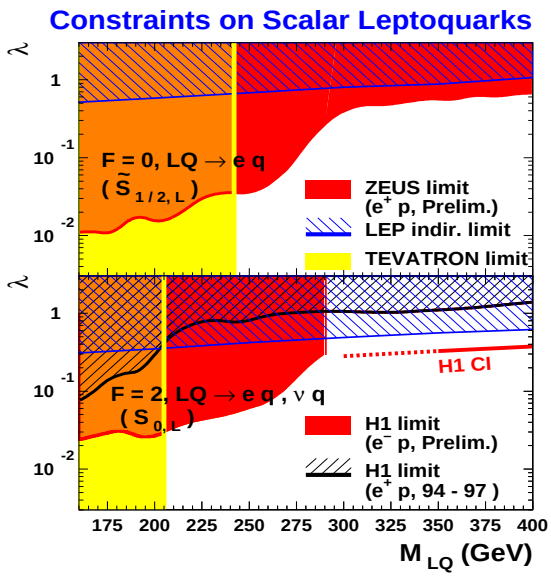

Fig. 37. Limits on coupling strength λ versus mass M_{LQ} for leptoquarks. The top plot shows limits for fermion number = 0 leptoquarks decaying into the eq final state from ZEUS. The lower plot shows limits from H1 for fermion number = 2 leptoquarks decaying into both eq and νq final states. Also shown are limits obtained from the Tevatron (yellow shaded area) and LEP (blue striped area). These leptoquark species have identical quantum numbers to squarks that violate R-parity.

One possible source of an excess of events with isolated leptons with missing transverse momentum would be from a flavour-changing neutral current process producing single top quarks. Both H1 and ZEUS have used the samples described above to put limits on the FCNC couplings of the γ to light quark-top quark vertices. The results are shown in Fig. 39. Also shown are the limits from LEP and CDF, which are complementary to those from HERA, in the sense that, since the Z-exchange cross section at HERA is so much smaller than that for γ exchange, the HERA data limit only the photon coupling.

9 HERA II physics

Since many of the physics results discussed above, particularly those at high Q^2, are statistics limited, there is a clear physics case for a significant increase in integrated luminosity for H1 and ZEUS. There are also other interesting physics investigations possible at HERA that have not yet been carried out. For example, there is a natural build-up of transverse polarisation of the lep-

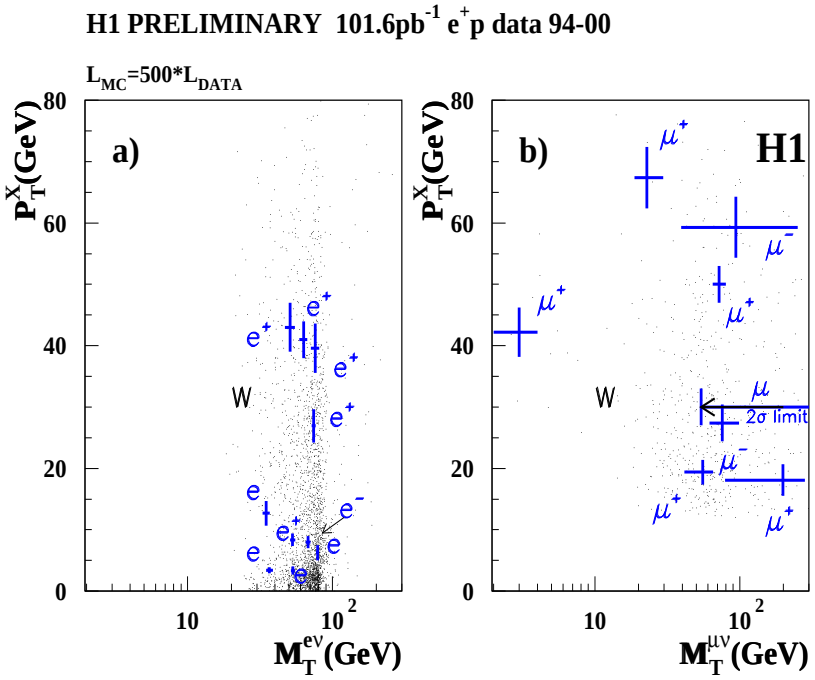

Fig. 38. Distribution of transverse mass versus the p_T of the hadronic system for H1 events containing a) isolated electrons and b) isolated muons. The dots show the distribution of Standard Model W Monte Carlo events corresponding to a luminosity 500 times that of the data.

ton beam in HERA that occurs through the Sokholov-Ternov effect [67]. As very successfully demonstrated at HERMES using gas targets, this transverse polarisation can be rotated into the longitudinal direction and utilised to do physics. The installation of spin rotators in H1 and ZEUS would allow polarisation studies to be carried out at very much higher Q^2. This is particularly interesting to study the chiral properties of the electroweak interaction. For these and several other reasons, it was decided to embark on a major upgrade of both the HERA accelerator and the H1 and ZEUS detectors. The aim of the HERA II programme is to produce a factor of approximately five increase in luminosity and accumulate 1 fb^{-1} of data with both electron and positron collisions in both longitudinal polarisation states.

The changes to the HERA accelerator include the replacement of 480 meters of the vacuum system and the design and installation of almost 80 magnets in the region around the H1 and ZEUS interaction points. In particular, superconducting quadrupole focussing elements were inserted inside both detectors to reduce the beam emittance and spin rotators were installed on either side of the H1 and ZEUS interaction regions.

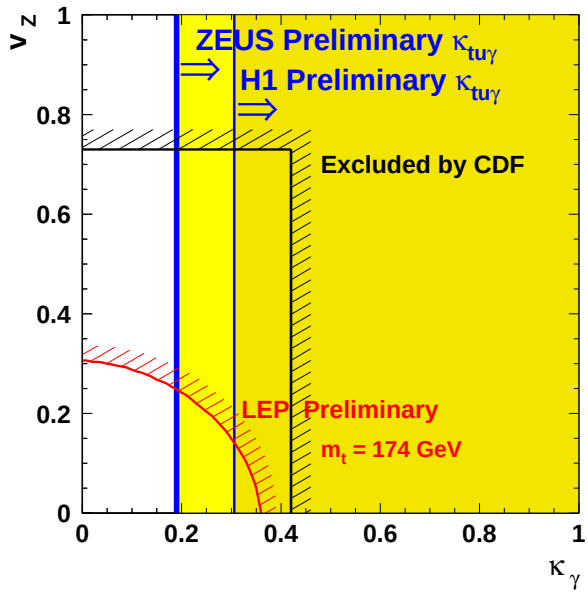

Fig. 39. Limits on flavour-changing neutral current coupling strength for single top production. Limits from H1 and ZEUS are plotted on the two-dimensional space of the photon and Z coupling strengths. Also shown are similar limits from the combined LEP experiments (to the right of the shaded curve) and from CDF (to the right of the black shaded lines).

Both the ZEUS and H1 detectors have undergone a massive programme of consolidation and repair work, as well as major detector upgrades. As an example, I discuss briefly the changes made to ZEUS; the general thrust of the upgrade is similar in the two detectors, although the details are different.

9.1 Upgrades to ZEUS for HERA II

The ZEUS upgrades have concentrated in three main areas: the vertex region; the forward direction; and the luminosity monitoring.

The vertex region The tagging of the large flux of heavy quarks (charm and beauty) produced at HERA II can be greatly enhanced by the installation of a high-precision charged-particle detector as close as possible to a thin beampipe. The ZEUS MVD [68,69] consists of 20 μm pitch n-type silicon-strip detectors with p^+-type implants. The readout pitch is 120 μm, leading to more than 200,000 readout channels, which are digitised by a custom-built clock, control and ADC system. The detectors are organised in two main groups: a "barrel", which surrounds the elliptical 2 mm-thick ($\sim$ 1.1% of a radiation length) aluminium-beryllium beam-pipe; and four "wheels",

consisting of wedge-shaped detectors mounted perpendicular to the beam-line in the forward direction from the interaction point. Figure 40 shows one half of the MVD before installation at DESY. In the barrel region, the ladders, each of which consists of five silicon detectors, and halves of the four forward "wheels", can be seen, as can the dense array of readout and services cables and the cooling system. The complete MVD was installed in ZEUS in April 2001 and has been fully integrated with the ZEUS DAQ system; both cosmic-ray and beam-related data have been taken.

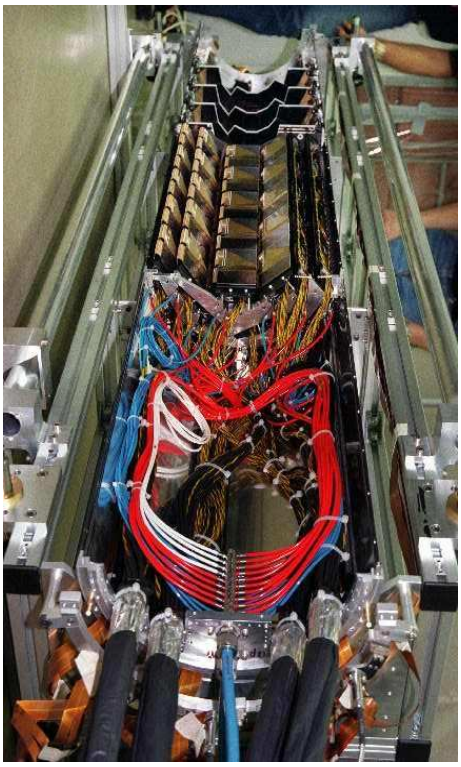

Fig. 40. A photograph of one half of the MVD, showing the barrel ladders, one half of each of the four forward wheels and the cables and services.

The physics programme addressed by the MVD is that of the flavour decomposition of the proton and photon and the search for physics beyond the Standard Model. The large increase in luminosity of HERA II, together with the ability to tag heavy-quark decays in the MVD, should greatly improve the measurement of F_2^c discussed in Section 4.4. After about 500 pb^{-1}, an uncertainty of around the 2% currently measured on F_2 should be obtained. In addition, b-quark production can be measured precisely; a Monte Carlo simulation [70] of a measurement of F_2^b/F_2^c after 500 pb^{-1} is shown in Fig. 41.

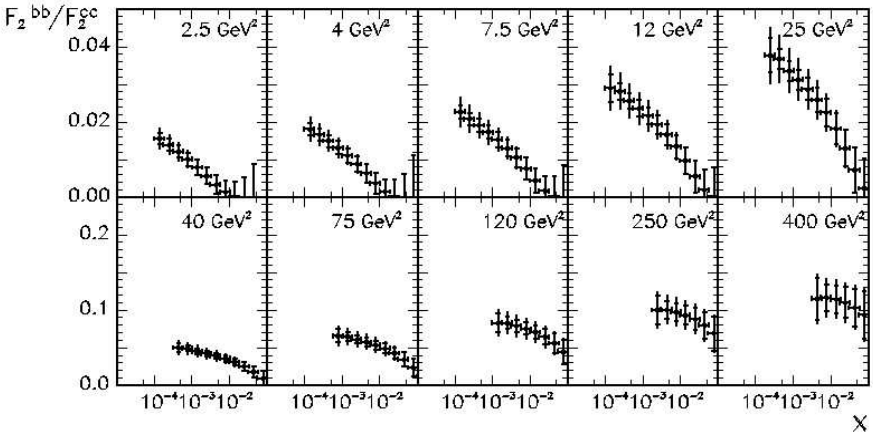

Fig. 41. The MC prediction for the ratio of the contribution to F_2 of b-quark to c-quark production in Q^2 bins as a function of x after 500 pb^{-1} of data at HERA II.

It should also be possible, from a combination of neutral and charged current measurements, to separate out the u, d, s, c, b and g contribution to F_2.

Charged-particle tracking in the forward direction The higher luminosity expected at HERA II will increase the number of very high-Q^2 events in which the electron or positron is scattered into the forward direction. It will also give access to rare processes, including possible physics beyond the Standard Model, which tend to have forward jets and/or leptons. The pattern-recognition capabilities of the ZEUS Forward Tracker have therefore been improved by the replacement of two layers of transition-radiation detector by layers of straw tubes. The straws are approximately 7.5 mm in diameter and range in length from around 20 cm to just over 1 m. They are constructed from two layers of 50 μm kapton foil coated with a 0.2 μm layer of aluminium, surrounding a 50 μm wire at the centre. The straws are arranged in wedges consisting of three layers rotated with respect to each other to give three-dimensional reconstruction. Each of the two "supermodules" consists of four layers of such wedges.

Luminosity monitor The measurement of luminosity at HERA II must cope with the greatly increased synchrotron-radiation background and the higher probability for multiple bremsstrahlung photons in one beam crossing. To compensate for this, two devices, with very different systematic uncertainties, have been constructed. Both devices use the information from a small calorimeter placed around 6 m from the interaction point which detects the

radiating electron. It is hoped that the reduction of systematic error that can be obtained from independent luminosity measurements using very different techniques will allow a precision of around 1% to be attained.

9.2 Polarisation

Polarisations of around 65% have been achieved at HERA I. It is hoped to increase the accuracy with which the polarisation can be measured to $\delta P/P \sim 2\%$ per bunch per minute. This will be achieved by a collaboration between H1, HERMES, ZEUS and the HERA machine in the POL2000 project. The collaboration has constructed two instruments, one to measure the longitudinal polarisation and the other to measure the transverse polarisation. Both detect asymmetries in back-scattered light from high-intensity polarised lasers.

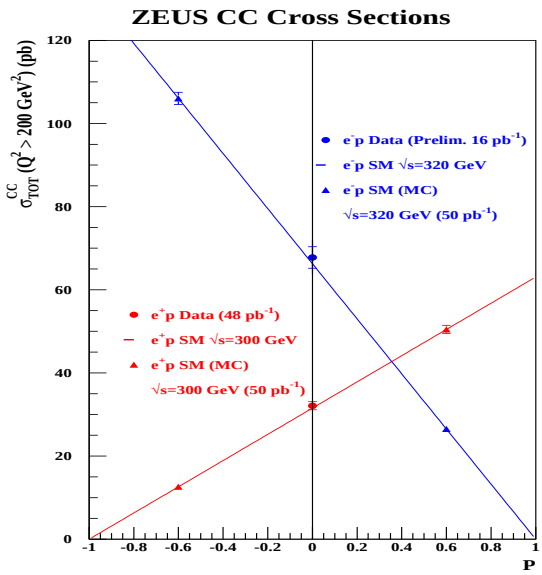

Fig. 42. The cross section for charged current interactions. The points at $P = 0$ are obtained from ZEUS preliminary results at the indicated centre-of-mass energies, while those at non-zero polarisation are Monte Carlo simulations of the expected accuracy in ZEUS assuming the Standard Model cross section for an integrated luminosity of 50 pb^{-1} per point.

The combination of high-precision measurements of both luminosity and polarisation will be important in a wide range of HERA II physics, particularly in the electroweak sector. The charged current cross section should

vanish for the appropriate combinations of lepton charge and polarisation. A measurement at three polarisations, such as shown in Fig. 42, even with an integrated luminosity of only 50 pb^{-1} per point, will provide an accurate test of this prediction and thereby give sensitivity to possible new currents outside the Standard Model.

Strong polarisation effects are also predicted at high Q^2 in neutral current interactions, where, e.g. at $Q^2 = 10^4$ GeV^2 and $x = 0.2$, there is a factor of two difference between the predicted cross sections for left- and right-handed electrons.

In addition to the use of precise luminosity and polarisation information in the study of electroweak processes, polarisation also offers an invaluable tool in the study of possible signals beyond the Standard Model. Varying the polarisation to reduce the cross sections of Standard Model processes can improve the signal to background for new physics signals, such as leptoquarks or supersymmetric particles that violate R parity, for which HERA will be competitive with the Tevatron for the next few years.

10 Summary

We have seen that the study of deep inelastic scattering has been seminal in the development of our current understanding of particle physics. In the last decade, HERA I has changed our perception of QCD out of all recognition. In many cases the precision of the data mandate NNL, or even high order, QCD predictions. The study of diffraction and the transition region between soft and hard physics may be the beginning of the era of quantitative study of the central problem of the strong interaction, confinement. The significant increase in expected luminosity and the use of new tools such as polarisation promise that HERA II physics should continue to provide both new results and surprises in the years to come.

Acknowledgements

I am grateful to George Zoupanos and his colleagues for organising a most stimulating summer school in beautiful surroundings and with outstanding hospitality.

References

1. See for example R.E. Taylor, Phil. Trans. R. Soc. Lond. **A 359** (2001) 225
2. E. Rutherford, Phil. Mag. **21** (1911) 669
3. H. Geiger and E. Marsden, Proc. Roy. Soc. Lond. **82** (1909) 495
4. F. Halzen and A.D. Martin, *Quarks and leptons*, John Wiley & sons, New York (1984)

5. J.D. Bjorken and E.A. Paschos, Phys. Rev. **165** (1969) 1975
6. C.G. Callan and D. Gross, Phys. Rev. Lett. **22** (1969) 156
7. See for example J.I. Friedman and H.W. Kendall, Ann. Rev. Nucl. Science **22** (1972) 203
8. G. Altarelli, R.K. Ellis and G. Martinelli, Nucl. Phys. **B 143** (1978) 521 and Nucl. Phys. **B 146** (1978) 544 (erratum)
9. H1 Collaboration, C. Adloff et al., Eur. Phys. J. **C 13** (2000) 609
10. H1 Collaboration, C. Adloff et al., Eur. Phys. J. **C 21** (2001) 33
11. ZEUS Collaboration, S. Chekanov et al., Eur. Phys. J. **C 21** (2001) 443
12. Particle Data Group, D.E. Groom et al., Eur. Phys. J. **C 15** (2000) 1
13. S. Bethke, J. Phys. G. **26** (2000) R27
14. ZEUS Collaboration, J. Breitweg et al., Eur. Phys. J. **C 12** (2000) 35
15. H1 Collaboration, C. Adloff et al., Phys. Lett. **B 528** (2002) 199
16. L.W. Whitlow et al., Phys. Lett. **B 282** (1992) 475
17. NMS Collaboration, M. Arneodo et al., Nucl. Phys. **B 483** (1997) 3
18. BCDMS Collaboration, A.C. Benvenuti et al., Phys. Lett. **B 223** (1989) 485
19. BCDMS Collaboration, A.C. Benvenuti et al., Phys. Lett. **B 237** (1990) 592
20. ZEUS Collaboration, J. Breitweg et al., Phys. Lett. **B 481** (2000) 213
21. L.N. Lipatov,Sov. J. Nucl. Phys. **20** (1975) 95
22. V.N. Gribov and L.N. Lipatov, Sov. J. Nucl. Phys. **15** (1972) 438
23. G. Altarelli and G. Parisi, Nucl. Phys. **B 126** (1977) 298
24. Yu.L. Dokshitzer, Sov. Phys. JETP **46** (1977) 641
25. R.K. Ellis, W.J. Stirling and B.R. Webber, *QCD and Collider Physics*, Cambridge Monographs on Particle Physics, Nuclear Physics and Cosmology, Volume 8, Cambridge University Press, Cambridge (1996)
26. E.A. Kuraev, L.N. Lipatov and V.S. Fadin, Phys. Lett. **B 60** (1975) 50
27. E.A. Kuraev, L.N. Lipatov and V.S. Fadin, Sov. Phys. JETP **44** (1976) 433
28. E.A. Kuraev, L.N. Lipatov and V.S. Fadin, Sov. Phys. JETP **45** (1977) 199
29. Ya.Ya. Balitsky and L.N. Lipatov, Sov. J. Nucl. Phys. **28** (1978) 822
30. M. Ciafaloni, Nucl. Phys. **B 296** (1988) 49
31. S. Catani, F. Fiorani and G. Marchesini, Phys. Lett. **B 234** (1990) 339
32. S. Catani, F. Fiorani and G. Marchesini, Nucl. Phys. **B 336** (1990) 18
33. L.V. Gribov, E.M. Levin and M.G. Ryskin, Phys. Rep. **100** (1983) 1
34. A.H. Mueller and J. Qiu, Nucl. Phys. **B 268** (1986) 427
35. A. Quadt, *Measurement and QCD Analysis of the Proton Structure Function F_2 from the 1994 HERA Data using the ZEUS Detector*, Ph.D. thesis, University of Oxford, 1997, RAL-TH-97-004
36. E. Levin, in Proceedings of the Ringberg Workshop, 'New Trends in HERA Physics', May 1999, hep-ph/9908379
37. M.G. Ryskin and E.M. Levin, Phys. Rep. **189** (1990) 267
38. B. Foster, Phil. Trans. R. Soc. Lond. **A 359** (2001) 325, and references therein
39. H.L. Lai et al., Eur. Phys. J. **C 12** (2000) 375
40. A.D. Martin et al., Eur. Phys. J. **C 23** (2002) 73
41. U.K. Yang and A. Bodek, Eur. Phys. J. **C 13** (2000) 241
42. M. Botje, Eur. Phys. J. **C 14** (2000) 285
43. CTEQ Collaboration, J. Pumplin et al., hep-ph/0201195
44. H1 Collaboration, C. Adloff et al., Eur. Phys. J. **C 21** (2001) 33
45. ZEUS Collaboration, S. Chekanov et al., to be submitted to Phys. Rev. D
46. S.A. Larin et al., Nucl. Phys. **B 492** (1997) 338

47. W.L. van Neerven and A. Vogt, Nucl. Phys. **B 568** (2000) 263
48. W.L. van Neerven and A. Vogt, Nucl. Phys. **B 588** (2000) 345
49. A.D. Martin et al., Eur. Phys. J. **C 18** (2000) 117
50. R.S. Thorne, Phys. Lett. **B 474** (2000) 373
51. R.S. Thorne, in Proceedings of Eight International Workshop on Deep Inelastic Scattering, DIS 2000, J.A. Gracey & T. Greenshaw (eds.), World Scientific, Singapore (2000), p. 174
52. K. Golec-Biernat and M. Wüsthoff, Phys. Rev. **D 59** (1999) 014017
53. K. Golec-Biernat and M. Wüsthoff, Phys. Rev. **D 60** (1999) 114023
54. ZEUS Collaboration, S. Chekanov et al., hep-ex/0203039, submitted to Eur. Phys. J. C.
55. ZEUS Collaboration, M. Derrick et al., Z. Phys. **C 73** (1997) 253
56. J. Bartels et al., Eur. Phys. J. **C 7** (1999) 443
57. ZEUS Collaboration, S. Chekanov et al., paper submitted to the International Europhysics Conference on High Energy Physics, Budapest, July 2001, Addendum to Abstract 548
58. L. Frankfurt, W. Koepf and M. Strikman, Phys. Rev **D 57** (1998) 512
59. A.D. Martin, M.G. Ryskin and T. Teubner, Phys. Rev. **D 62** (2000) 14022
60. J. Forshaw and G. Poludniowski, hep-ph/0107068
61. P.R.B. Saull, talk at International Europhysics Conference on High Energy Physics, Tampere, July 1999
62. H1 Collaboration, C. Adloff et al., Phys. Lett. **B 517** (2001) 47
63. L. Frankfurt, A. Freund and M. Strikman Phys. Rev. **D 58** (1998) 114001 and erratum, Phys. Rev. **D 59** (1999) 119901E
64. A. Donnachie and H.G. Dosch, Phys. Lett. **B 502** (2001) 74
65. L. Frankfurt, M. McDermott and M. Strikman, J. High Energy Phys. **103** (2001) 45
66. H1 Collaboration, C. Adloff et al., Eur. Phys. J. **C19** (2001) 269
67. A.A. Sokholov and M. Ternov, Sov. Phys. Dokl. **8** (1964) 1203
68. A. Garfagnini, Nucl. Instr. and Meth. **A435** (1999) 34
69. E. Koffeman, Nucl. Instr. and Meth. **A473** (2001) 26
70. K. Daum et al., in Proceedings of the Workshop on Future Physics at HERA, ed. A. De Roeck, G. Ingleman and R. Klanner, Vol. 1, p. 89, DESY, Hamburg, (1996).